

# The escape of heavy atoms from the ionosphere of HD209458b. I. A photochemical-dynamical model of the thermosphere.

T. T. Koskinen<sup>a,\*</sup>, M. J. Harris<sup>b</sup>, R. V. Yelle<sup>a</sup>, P. Lavvas<sup>c</sup>

<sup>a</sup>*Lunar and Planetary Laboratory, University of Arizona, 1629 E. University Blvd., Tucson, AZ 85721, USA*

<sup>b</sup>*Department of Physics and Astronomy, University College London, Gower Street, London WC1E 6BT, UK*

<sup>c</sup>*Groupe de Spectrométrie Moléculaire et Atmosphérique UMR CNRS 6089, Université Reims Champagne-Ardenne, 51687, France*

---

## Abstract

The detections of atomic hydrogen, heavy atoms and ions surrounding the extrasolar giant planet (EGP) HD209458b constrain the composition, temperature and density profiles in its upper atmosphere. Thus the observations provide guidance for models that have so far predicted a range of possible conditions. We present the first hydrodynamic escape model for the upper atmosphere that includes all of the detected species in order to explain their presence at high altitudes, and to further constrain the temperature and velocity profiles. This model calculates the stellar heating rates based on recent estimates of photoelectron heating efficiencies, and includes the photochemistry of heavy atoms and ions in addition to hydrogen and helium. The composition at the lower boundary of the escape model is constrained

---

\*Corresponding author. Fax: +1 (520) 621 4933  
*Email address:* `tommi@lpl.arizona.edu` (T. T. Koskinen)

by a full photochemical model of the lower atmosphere. We confirm that molecules dissociate near the 1  $\mu$ bar level, and find that complex molecular chemistry does not need to be included above this level. We also confirm that diffusive separation of the detected species does not occur because the heavy atoms and ions collide frequently with the rapidly escaping H and H<sup>+</sup>. This means that the abundance of the heavy atoms and ions in the thermosphere simply depends on the elemental abundances and ionization rates. We show that, as expected, H and O remain mostly neutral up to at least 3  $R_p$ , whereas both C and Si are mostly ionized at significantly lower altitudes. We also explore the temperature and velocity profiles, and find that the outflow speed and the temperature gradients depend strongly on the assumed heating efficiencies. Our models predict an upper limit of 8,000 K for the mean (pressure averaged) temperature below 3  $R_p$ , with a typical value of 7,000 K based on the average solar XUV flux at 0.047 AU. We use these temperature limits and the observations to evaluate the role of stellar energy in heating the upper atmosphere.

*Keywords:* Extra-solar planets, Aeronomy, Atmospheres, composition, Photochemistry

---

## 1. Introduction

The detection of hot atomic hydrogen in the upper atmosphere of HD209458b (Vidal-Madjar et al., 2003, 2004) has inspired numerous attempts to model physical and chemical processes in highly irradiated atmospheres, including

5 rapid escape as one of the most challenging aspects. Subsequent detection of  
6 heavy atoms and ions (Vidal-Madjar et al., 2004; Linsky et al., 2010) point  
7 out the need for more complex models that include the chemistry associated  
8 with these species as well as the collision coupling between them and the ma-  
9 jor species. Indeed, close-in extrasolar planets offer a natural laboratory to  
10 constrain the theory of rapid escape, including hydrodynamic escape. This  
11 is important because aspects of the theory are controversial, and yet rapid  
12 escape is believed to have played a role in shaping the early evolution of the  
13 atmospheres in the solar system (e.g., Zahnle and Kasting, 1986; Hunten et  
14 al., 1987). Escape may also be a crucial factor in determining atmospheric  
15 conditions and habitability of super-Earths and Earth-like planets around  
16 M dwarfs (e.g., Tarter et al., 2007) that may be amenable to spectroscopic  
17 studies in the near future (e.g., Charbonneau et al., 2009).

18 The basic ideas about the nature of the upper atmospheres around close-in  
19 EGPs were laid out almost as soon as the first planet, 51 Peg b (Mayor et al.,  
20 1995), was detected. For instance, Coustenis et al. (1998) argued that heating  
21 by the stellar EUV radiation and interaction with the stellar wind leads to  
22 high temperatures of several thousand Kelvins in the upper atmosphere and  
23 exosphere of close-in EGPs. They also suggested that the upper atmosphere  
24 is primarily composed of atoms and ions, and that hydrodynamic escape  
25 might be able to drag species heavier than H and He into the exosphere. At  
26 the same time, Schneider et al. (1998) argued that material escaping from  
27 the atmospheres of close-in EGPs would form a potentially observable comet-

28 like tail. When Vidal-Madjar et al. (2003, 2004) detected the transits of  
29 HD209458b in the stellar FUV emission lines, they also argued that the planet  
30 is followed by comet-like tail of escaping hydrogen, and that hydrodynamic  
31 escape is required to drag oxygen and carbon atoms to the thermosphere.

32 The model of Yelle (2004, 2006) was the first attempt to model the aeron-  
33 omy and escape processes in detail and most of the assumptions in that  
34 work have been adopted by subsequent investigators. It solved the vertical  
35 equations of continuity, momentum, and energy for an escaping atmosphere,  
36 including photochemistry in the ionosphere and transfer of stellar XUV ra-  
37 diation. Based on a composition of hydrogen and helium, the results demon-  
38 strated that  $\text{H}_2$  dissociates in the thermosphere, which at high altitudes is  
39 dominated by H and  $\text{H}^+$ . The model also showed that stellar heating leads  
40 to temperatures of  $\sim 10,000$  K in the upper atmosphere, and predicted an  
41 energy-limited mass loss rate of  $4.7 \times 10^7 \text{ kg s}^{-1}$  (Yelle, 2006).

42 Yelle (2004) argued that conditions beyond  $\sim 3 R_p$  were too complex and  
43 uncertain to be modeled reliably and therefore chose an upper boundary at 3  
44  $R_p$ , rather than at infinity, as adopted in early solar wind models. This led to  
45 a requirement for boundary conditions for the fluid equations at a finite ra-  
46 dius. Yelle (2004) required consistency between fluid and kinetic simulations,  
47 based on the well established fact that kinetic and fluid approaches provide  
48 consistent results for the escape flux (e.g., Lemaire and Scherer, 1973). This  
49 led to subsonic velocities of a few  $\text{km s}^{-1}$  in his model – although the presence  
50 of a sonic point at a higher altitude was not ruled out.

51 Many other models for the upper atmospheres of close-in EGPs have  
52 been published (e.g., Lammer et al., 2003; Lecavelier des Etangs et al., 2004;  
53 Jaritz et al., 2005; Tian et al., 2005; Erkaev et al., 2007; Garcia Munoz, 2007;  
54 Schneider et al., 2007; Penz et al., 2008; Holström et al., 2008; Murray-Clay et  
55 al., 2009; Stone and Proga, 2009; Guo, 2011; Trammell et al., 2011). These in-  
56 clude one-dimensional, two-dimensional, and three-dimensional models that  
57 make different assumptions regarding heating efficiency, the effect of stellar  
58 tides, photochemistry, and the escape mechanism. Despite significant dif-  
59 ferences in the temperature and velocity profiles, almost all of the existing  
60 models agree that close-in EGPs such as HD209458b are surrounded by an  
61 extended, hot thermosphere that is undergoing some form of escape. Most of  
62 the models to date concentrate on the distribution of H and H<sup>+</sup> in the upper  
63 atmosphere. Garcia Munoz (2007) developed the only model to address the  
64 presence of O and C<sup>+</sup> in the thermosphere (Vidal-Madjar et al., 2004; Linsky  
65 et al., 2010). This model is otherwise similar to Yelle (2004), but it includes  
66 the photochemistry of heavy ions, atoms, molecules, and molecular ions. It  
67 also extends to higher altitudes, and includes the effect of substellar tidal  
68 forces and stellar wind, albeit in an approximate manner.

69 Koskinen et al. (2007a,b) developed a three-dimensional model for the  
70 thermospheres of EGPs at wide orbits. They pointed out that the atmo-  
71 spherics of close-in EGPs do not escape hydrodynamically unless they receive  
72 enough stellar XUV energy to dissociate molecules in the EUV heating layer  
73 below the exobase. Although their results are limited to the specific case of

74 H<sub>2</sub>, they can be generalized as follows. The most important molecules H<sub>2</sub>  
75 (through the formation of H<sub>3</sub><sup>+</sup>), CO, H<sub>2</sub>O, and CH<sub>4</sub> act as strong infrared  
76 coolants in the thermosphere. High temperatures and rapid escape are only  
77 possible once these molecules are dissociated. Koskinen et al. (2007b) showed  
78 that H<sub>2</sub> dissociates in the thermosphere of a Jupiter-type planet orbiting a  
79 Sun-like star within 0.2 AU. Once H<sub>2</sub> dissociates, it is reasonable to assume  
80 that other molecules dissociate too. At this point the pressure scale height  
81 is enhanced by a factor of ~10 when H becomes the dominant species in the  
82 thermosphere and temperatures reach 10,000 K.

83 It should be noted that a composition of H and H<sup>+</sup> with high temper-  
84 atures does not guarantee that the atmosphere escapes hydrodynamically.  
85 For instance, Koskinen et al. (2009) showed that hydrodynamic escape is ex-  
86 tremely unlikely to occur on a planet such as HD17156b because of its high  
87 mass and eccentric orbit. These types of results have implications on statis-  
88 tical studies that characterize the escape of planetary atmospheres by relying  
89 on the so-called energy-limited escape (e.g., Watson et al., 1981; Lecavelier  
90 des Etangs, 2007; Sanz-Forcada et al., 2010). These studies often include an  
91 efficiency factor in the mass loss rate that is based on the heating efficiency  
92 of the upper atmosphere (e.g., Lammer et al., 2009). Unless the atmosphere  
93 is escaping rapidly, the heating efficiency could be considerably larger than  
94 the fraction of energy that actually powers escape through adiabatic cool-  
95 ing. Under diffusion-limited escape or in the Jeans regime the energy-limited  
96 escape rate is just an upper limit and the true escape rate can be lower.

97 Ideally, the uncertainties in the models can be limited by detailed obser-  
98 vations of the escaping species. At present, multiple observations are only  
99 available for HD209458b, and they reveal the presence of H, O, C<sup>+</sup>, and Si<sup>2+</sup>  
100 at high altitudes in the thermosphere (Vidal-Madjar et al., 2003, 2004; Lin-  
101 sky et al., 2010). Visible and infrared observations have also revealed the  
102 presence of Na, H<sub>2</sub>O, CH<sub>4</sub>, and CO<sub>2</sub> in the lower atmosphere (Charbonneau  
103 et al., 2002; Knutson et al., 2008; Swain et al., 2009). Taken together, these  
104 observations are beginning to reveal the composition and thermal structure  
105 in the atmosphere of HD209458b. The purpose of the current paper is to  
106 characterize the density profiles of all of the detected species in the ther-  
107 mosphere, and to explain the presence of the heavy atoms and ions at high  
108 altitudes in the upper atmosphere. The results can be used to infer some  
109 basic properties of the atmosphere.

110 To this end, we introduce a one-dimensional escape model for the upper  
111 atmosphere of HD209458b that includes the photochemistry of heavy atoms  
112 and ions. As pointed out above, previous models agree broadly on the quali-  
113 tative nature of the thermosphere but the temperature, density, and velocity  
114 profiles predicted by them differ significantly (see Section 3.1). Some authors  
115 have argued that the density of H in the thermosphere is not sufficient to  
116 explain the observed transit depths (see Koskinen et al., 2010a, for a review),  
117 thus lending support to alternative interpretations of the observations such  
118 as the presence of energetic neutral atoms (Holström et al., 2008) or a comet-  
119 like tail of hydrogen shaped by radiation pressure (Vidal-Madjar et al., 2003).

120 Accurate modeling of the thermosphere is required to enable better judgment  
121 between different explanations of the observations.

122 The differences between previous models arise from different assumptions  
123 regarding heating rates and boundary conditions. In addition to modeling  
124 the density profiles of the detected heavy species, we have improved these  
125 aspects of the calculations in our work. For instance, the lower boundary  
126 conditions are constrained by results from a detailed photochemical model  
127 of the lower atmosphere (Lavvas et al., *in preparation*). With regard to the  
128 upper boundary conditions, we demonstrate that for HD209458b the extrap-  
129 olated ‘outflow’ boundary conditions (e.g., Tian et al., 2005) are consistent  
130 with recent results from kinetic theory (Volkov et al., 2011a,b) as long as  
131 the upper boundary is at a sufficiently high altitude – although uncertainties  
132 regarding the interaction of the atmosphere with the stellar wind may limit  
133 the validity of both boundary conditions. We highlight the effect of heat-  
134 ing efficiency and stellar flux on the density and temperature profiles, and  
135 constrain the likely heating rates by using photoelectron heating efficiencies  
136 based on the results of Cecchi-Pestellini et al. (2009) and our own estimates  
137 (Section 3.1). As a result we provide a robust qualitative description of the  
138 density profiles, and constrain the mean temperature and velocity profile  
139 in the thermosphere. A second paper by Koskinen et al. (2012) (Paper II)  
140 compares our results directly with the observations.



141 **2. Methods**

142 *2.1. Hydrodynamic model*

143 We use a one-dimensional escape model for HD209458b ( $R_p = 1.32 R_J$ ,  
 144  $M_p = 0.69 M_J$ ,  $a = 0.047$  AU) that is similar to the models of Yelle (2004)  
 145 and Garcia Munoz (2007). Because such models are extensively discussed  
 146 in the literature, we include only a brief overview of the model here, with  
 147 the emphasis on how it differs from previous work. The model solves the  
 148 one-dimensional equations of motion for an escaping atmosphere composed  
 149 of several neutral and ionized species:

$$\frac{\partial \rho_s}{\partial t} + \frac{1}{r^2} \frac{\partial}{\partial r} (r^2 \rho_s v) + \frac{1}{r^2} \frac{\partial}{\partial r} (r^2 F_s) = \sum_t R_{st} \quad (1)$$

$$\frac{\partial(\rho v)}{\partial t} + \frac{1}{r^2} \frac{\partial}{\partial r} (r^2 \rho v^2) = -\rho g - \frac{\partial p}{\partial r} + f_\mu \quad (2)$$

$$\begin{aligned} \frac{\partial(\rho E)}{\partial t} + \frac{1}{r^2} \frac{\partial}{\partial r} (r^2 \rho E v) &= \rho Q_R - p \frac{1}{r^2} \frac{\partial}{\partial r} (r^2 v) \\ &+ \frac{1}{r^2} \frac{\partial}{\partial r} \left( r^2 \kappa \frac{\partial T}{\partial r} \right) + \Phi_\mu \end{aligned} \quad (3)$$

150 where  $\rho_s$  is the density of species  $s$ ,  $v$  is the vertical velocity,  $F_s$  is the diffusive  
 151 flux of species  $s$ ,  $R_{st}$  is the net chemical source term for species  $s$ ,  $f_\mu$  is a  
 152 force term arising from viscous acceleration,  $E = c_v T$  is the specific internal  
 153 energy of the gas,  $Q_R$  is the specific net radiative heating rate,  $\kappa$  is the  
 154 coefficient of heat conduction, and  $\Phi_\mu$  is the viscous dissipation functional  
 155 (e.g., O'Neill and Chorlton, 1989). The total density and pressure are given  
 156 by  $\rho = \sum_s \rho_s$  and  $p = \sum_s n_s k T$ , respectively, where electrons contribute to

157 the total pressure.

158 We assumed equal temperatures for the neutral species, ions and elec-  
159 trons, and calculated the electron density at each altitude from the require-  
160 ment of charge neutrality. The model solves separate continuity equations  
161 for each species, but treats the atmosphere otherwise as a single fluid. The  
162 differences in the velocities of the individual species are taken into account by  
163 including the diffusive flux  $F_s$ . We calculated the fluxes by solving simulta-  
164 neous equations for multiple species based on the diffusion equation given by  
165 Chapman and Cowling (1970) (equation 18.2,6, p.344). We also included a  
166 force term due to the ambipolar electric field given by  $eE = -(1/n_e)dp_e/dr$ ,  
167 where the subscript  $e$  refers to electrons, that can be important in highly  
168 ionized flows. The collision terms account for neutral-neutral, resonant and  
169 non-resonant ion-neutral, and Coulomb collisions. This method is in princi-  
170 ple similar to those of Yelle (2004) and Garcia Munoz (2007). We verify that  
171 the single temperature and diffusion approximations are valid for HD209458b  
172 based on our results in Section 3.2.2.

173 The model includes heat conduction and terms due to viscosity in both  
174 the momentum and energy equations. Thus the equations are consistent  
175 with the level of approximation in the Navier-Stokes (NS) equations. The  
176 NS equations themselves are a simplification of the 13-moment solution to the  
177 Boltzmann equation (e.g., Gombosi, 1994) that is valid when the Knudsen  
178 number  $Kn = \Lambda/L \ll 1$ , where  $\Lambda$  is the mean free path and  $L$  is the typ-  
179 ical length scale for significant changes in density or temperature. Broadly

180 speaking, the equations are valid below the exobase, and terms due to heat  
181 conduction and viscosity gain significance as  $Kn \rightarrow 1$ . We note that the  
182 exobase on HD209458b is typically located at a very high altitude (see Sec-  
183 tion 3.1), and viscosity and heat conduction are not particularly important.

184 We included species such as H, H<sup>+</sup>, He, He<sup>+</sup>, C, C<sup>+</sup>, O, O<sup>+</sup>, N, N<sup>+</sup>,  
185 Si, Si<sup>+</sup>, Si<sup>2+</sup>, and electrons in the hydrodynamic model. We also generated  
186 simulations that included Mg, Mg<sup>+</sup>, Na, Na<sup>+</sup>, K, K<sup>+</sup>, S, and S<sup>+</sup>, but the  
187 presence of these species did not affect the density profiles of H, O, C<sup>+</sup>, or Si<sup>2+</sup>  
188 significantly. The model includes photoionization, thermal ionization, and  
189 charge exchange between atoms and ions. The reaction rate coefficients for  
190 these processes are listed in Table 1. Multiply charged ions were included only  
191 if the ionization potential of their parent ion was sufficiently low compared to  
192 the thermal energy and radiation field in the upper atmosphere. We note that  
193 our model also includes impact ionization by thermal electrons. In general,  
194 this can be important for species with low ionization potential such as alkali  
195 metals (e.g., Batygin and Stevenson, 2010), although we find photoionization  
196 to be more significant in the thermosphere (see Section 3.2).

197 In order to simulate photochemistry in a numerically robust fashion, we  
198 coupled the dynamical model with the ASAD chemistry integrator developed  
199 at the University of Cambridge (Carver et al., 1997). In most cases we used  
200 the IMPACT integration scheme that is provided by ASAD. We did not  
201 include any molecules in the present simulations, and thus placed the lower  
202 boundary of the hydrodynamic model at  $p_0 = 1 \mu\text{bar}$  (see Section 2.1.1).

203 Molecular chemistry is not significant in the thermosphere, where our results  
 204 agree qualitatively with Garcia Munoz (2007) despite simpler chemistry (see  
 205 Section 3.2). This is an important result because it implies that complex  
 206 molecular photochemistry does not need to be included in the models for the  
 207 thermosphere. However, the chemistry of molecular ions may be important  
 208 on HD209458b below the 0.1  $\mu$ bar level and it needs to be studied in greater  
 209 detail.

Table 1: Reaction rate coefficients

Reaction	Rate ( $\text{cm}^3 \text{s}^{-1}$ )	Reference
P1 $\text{H} + h\nu \rightarrow \text{H}^+ + e$		(Hummer and Seaton, 1963)
P2 $\text{He} + h\nu \rightarrow \text{He}^+ + e$		(Yan et al., 1998)
P3 $\text{O} + h\nu \rightarrow \text{H}^+ + e$		(Verner et al., 1996)
P4 $\text{C} + h\nu \rightarrow \text{C}^+ + e$		(Verner et al., 1996)
P5 $\text{N} + h\nu \rightarrow \text{N}^+ + e$		(Verner et al., 1996)
P6 $\text{Si} + h\nu \rightarrow \text{Si}^+ + e$		(Verner et al., 1996)
P7 $\text{Si}^+ + h\nu \rightarrow \text{Si}^{2+} + e$		(Verner et al., 1996)
R1 $\text{H}^+ + e \rightarrow \text{H} + h\nu$	$4.0 \times 10^{-12} (300/T_e)^{0.64}$	(Storey and Hummer, 1995)
R2 $\text{He}^+ + e \rightarrow \text{He} + h\nu$	$4.6 \times 10^{-12} (300/T_e)^{0.64}$	(Storey and Hummer, 1995)
R3 $\text{H} + e \rightarrow \text{H}^+ + e + e$	$2.91 \times 10^{-8} \left( \frac{1}{0.232+U} \right) U^{0.39} \exp(-U)$ , $U = 13.6/E_e(\text{eV})$	(Voronov, 1997)
R4 $\text{He} + e \rightarrow \text{He}^+ + e + e$	$1.75 \times 10^{-8} \left( \frac{1}{0.180+U} \right) U^{0.35} \exp(-U)$ , $U = 24.6/E_e(\text{eV})$	(Voronov, 1997)
R5 $\text{H} + \text{He}^+ \rightarrow \text{H}^+ + \text{He}$	$1.25 \times 10^{-15} (300/T)^{-0.25}$	(Glover and Jappsen, 2007)
R6 $\text{H}^+ + \text{He} \rightarrow \text{H} + \text{He}^+$	$1.75 \times 10^{-11} (300/T)^{0.75} \exp(-128,000/T)$	(Glover and Jappsen, 2007)
R7 $\text{O} + e \rightarrow \text{O}^+ + e + e$	$3.59 \times 10^{-8} \left( \frac{1}{0.073+U} \right) U^{0.34} \exp(-U)$ , $U = 13.6/E_e(\text{eV})$	(Voronov, 1997)
R8 $\text{C} + e \rightarrow \text{C}^+ + e + e$	$6.85 \times 10^{-8} \left( \frac{1}{0.193+U} \right) U^{0.25} \exp(-U)$ , $U = 11.3/E_e(\text{eV})$	(Voronov, 1997)
R9 $\text{O}^+ + e \rightarrow \text{O} + h\nu$	$3.25 \times 10^{-12} (300/T_e)^{0.66}$	(Woodall et al., 2007)
R10 $\text{C}^+ + e \rightarrow \text{C} + h\nu$	$4.67 \times 10^{-12} (300/T_e)^{0.60}$	(Woodall et al., 2007)
R11 $\text{C}^+ + \text{H} \rightarrow \text{C} + \text{H}^+$	$6.30 \times 10^{-17} (300/T)^{-1.96} \exp(-170,000/T)$	(Stancil et al., 1998)
R12 $\text{C} + \text{H}^+ \rightarrow \text{C}^+ + \text{H}$	$1.31 \times 10^{-15} (300/T)^{-0.213}$	(Stancil et al., 1998)
R13 $\text{C} + \text{He}^+ \rightarrow \text{C}^+ + \text{He}$	$2.50 \times 10^{-15} (300/T)^{-1.597}$	(Glover and Jappsen, 2007)
R14 $\text{O}^+ + \text{H} \rightarrow \text{O} + \text{H}^+$	$5.66 \times 10^{-10} (300/T)^{-0.36} \exp(8.6/T)$	(Woodall et al., 2007)
R15 $\text{O} + \text{H}^+ \rightarrow \text{O}^+ + \text{H}$	$7.31 \times 10^{-10} (300/T)^{-0.23} \exp(-226.0/T)$	(Woodall et al., 2007)
R16 $\text{N} + e \rightarrow \text{N}^+ + e + e$	$4.82 \times 10^{-8} \left( \frac{1}{0.0652+U} \right) U^{0.42} \exp(-U)$ , $U = 14.5/E_e(\text{eV})$	(Voronov, 1997)
R17 $\text{N}^+ + e \rightarrow \text{N} + h\nu$	$3.46 \times 10^{-12} (300/T_e)^{0.608}$	(Aldrovandi and Pequignot, 1973)
R18 $\text{Si} + e \rightarrow \text{Si}^+ + e + e$	$1.88 \times 10^{-7} \left( \frac{1+\sqrt{U}}{0.376+U} \right) U^{0.25} \exp(-U)$ , $U = 8.2/E_e(\text{eV})$	(Voronov, 1997)
R19 $\text{Si}^+ + e \rightarrow \text{Si} + h\nu$	$4.85 \times 10^{-12} (300/T_e)^{0.60}$	(Aldrovandi and Pequignot, 1973)
R20 $\text{Si}^+ + e \rightarrow \text{Si}^{2+} + e + e$	$6.43 \times 10^{-8} \left( \frac{1+\sqrt{U}}{0.632+U} \right) U^{0.25} \exp(-U)$ , $U = 16.4/E_e(\text{eV})$	(Voronov, 1997)
R21 $\text{Si}^{2+} + e \rightarrow \text{Si}^+ + h\nu$	$1.57 \times 10^{-11} (300/T_e)^{0.786}$	(Aldrovandi and Pequignot, 1973)
R22 $\text{H}^+ + \text{Si} \rightarrow \text{H} + \text{Si}^+$	$7.41 \times 10^{-11} (300/T)^{-0.848}$	(Glover and Jappsen, 2007)
R23 $\text{He}^+ + \text{Si} \rightarrow \text{He} + \text{Si}^+$	$3.30 \times 10^{-9}$	(Woodall et al., 2007)
R24 $\text{C}^+ + \text{Si} \rightarrow \text{C} + \text{Si}^+$	$2.10 \times 10^{-9}$	(Woodall et al., 2007)
R25 $\text{H} + \text{Si}^{2+} \rightarrow \text{H}^+ + \text{Si}^+$	$2.20 \times 10^{-9} (300/T)^{-0.24}$	(Kingdon and Ferland, 1996)
R26 $\text{H}^+ + \text{Si}^+ \rightarrow \text{H} + \text{Si}^{2+}$	$7.37 \times 10^{-10} (300/T)^{-0.24}$	(Kingdon and Ferland, 1996)

210 The upper atmosphere is heated by stellar XUV radiation. We simulated

211 heating and photoionization self-consistently by using the model density pro-  
212 files and the UV spectrum of the average Sun. The spectrum covers wave-  
213 lengths between 0.1–3000 Å. The XUV spectrum between 0.1–1050 Å was  
214 generated by the SOLAR2000 model (Tobiska et al., 2000). It includes strong  
215 emission lines separately and weaker lines binned by 50 Å. The Lyman  $\alpha$  line  
216 was included with a wavelength spacing of 0.5 Å from Lemaire et al. (2005)  
217 and the rest of the spectrum was taken from Woods and Rottman (2002).  
218 We assumed that most of the Lyman  $\alpha$  radiation absorbed by H is reso-  
219 nantly scattered and does not contribute significantly to the heating of the  
220 atmosphere. This is because the lifetime of the 2p state of H is only 1.6 ns,  
221 compared with the typical collision timescale of  $\sim 1$  s near the temperature  
222 peak in the thermosphere of HD209458b.

223       References for photoabsorption cross sections of the different species are  
224 included in Table 1. In general, we divided the incident stellar flux by a factor  
225 of 4 to account for uniform redistribution of energy around the planet. This  
226 is expected to be approximately valid in the lower thermosphere based on the  
227 three-dimensional simulations of Koskinen et al. (2010b). In the extended  
228 upper thermosphere, on the other hand, radiation passes through to the night  
229 side and leaves only a small region free of direct heating (e.g., see Figure 2  
230 of Koskinen et al., 2007b). The current model also includes heating due to  
231 photoabsorption by C, O, N, and metals. This is relatively insignificant –  
232 although it leads to some additional heating in the lower thermosphere by  
233 FUV radiation.

234 Heating of the thermosphere is mostly driven by photoionization and  
235 the generation of photoelectrons, although direct excitation of atoms and  
236 molecules may also play a role. Photoelectrons excite, ionize, and dissociate  
237 atoms and molecules until they lose enough energy and become thermalized  
238 i.e., share their energy with thermal electrons in Coulomb collisions. Thermal  
239 electrons share their energy with ions and eventually, the neutral atmosphere.  
240 In highly ionized atmospheres such as on HD209458b the photoelectron heat-  
241 ing efficiency can be close to 100 % (Cecchi-Pestellini et al., 2009), depending  
242 on the energy of the photoelectrons. We used scaled heating efficiencies that  
243 depend on photoelectron energy to estimate the net heating efficiency in the  
244 atmosphere (Section 3.1).

245 Generally, we refer to two different definitions of heating efficiency in Sec-  
246 tion 3.1 in order to highlight the effect of heating efficiency on the tempera-  
247 ture and velocity profiles. The net heating efficiency  $\eta_{\text{net}}$  is defined simply as  
248 the fraction of the absorbed stellar energy that heats the atmosphere. Pho-  
249 toelectron heating efficiency, on the other hand, applies to photoelectrons  
250 with energy  $E_p = h\nu - I_s$  where  $I_s$  is the ionization potential of species  
251  $s$  and  $h\nu$  is the energy of the ionizing photon. The photoelectron heating  
252 efficiency is the fraction of  $E_p$  that heats the thermosphere, and it is gen-  
253 erally higher than  $\eta_{\text{net}}$  because it does not account for recombination. The  
254 net heating efficiency is often used to calculate mass loss rates for extrasolar  
255 planets (e.g., Lammer et al., 2009). Therefore it is important not to confuse  
256 these two definitions of heating efficiency. We included radiative cooling by

257 recombination under the assumption that the thermosphere is optically thin  
258 to the emitted photons. This implies that the ionization potential energy  $I_s$   
259 never contributes to heating at any levels. We also considered the influence  
260 of Lyman  $\alpha$  cooling by excited H, although this cooling rate is uncertain and  
261 likely to be low for HD209458b. We discuss the effect of different cooling  
262 rates further in Section 3.1.

### 263 *2.1.1. Lower boundary conditions*

264 As stated above, we placed the lower boundary of the hydrodynamic  
265 model at  $p_0 = 1 \mu\text{bar}$  and did not include  $\text{H}_2$  or other molecules in the model.  
266 This decision was motivated by photochemical calculations for HD209458b  
267 (Lavvas et al., *in preparation*) that we used to constrain the lower bound-  
268 ary condition. The photochemical model was originally developed for the  
269 atmosphere of Titan (Lavvas et al., 2008a,b) but it was recently expanded  
270 to simulate EGP atmospheres. It calculates the chemical composition from  
271 the deep troposphere (1000 bar) up to the thermosphere above the 0.1 nbar  
272 level by solving the coupled continuity equations for all species based on a  
273 database of  $\sim 1,500$  reaction rate coefficients and 103 photolysis processes.  
274 Forward and reverse rates are included for each reaction with the ratio of  
275 the rate coefficients defined by thermochemical data. Thus, the results are  
276 consistent with thermochemical equilibrium at deep atmospheric levels but  
277 differences develop at higher altitudes due to photolysis, diffusion, and eddy  
278 mixing. At the lower boundary the chemical abundances of the main species

279 (H, C, N, and O) are set to their thermodynamic equilibrium values and,  
280 depending on the vertical temperature profile and their abundances, species  
281 are allowed to condense.

282 Figure 1 shows the mixing ratios of H<sub>2</sub>, H, H<sub>2</sub>O, O, CH<sub>4</sub>, CO, CO<sub>2</sub>, and  
283 C as a function of altitude from the photochemical model. In general, the  
284 results are similar to those of Moses et al. (2011). The H<sub>2</sub>/H transition is  
285 located near 1  $\mu$ bar. At lower pressures, the mixing ratio of H<sub>2</sub> decreases  
286 rapidly with altitude and falls below 0.1 above the 0.1  $\mu$ bar level. In agree-  
287 ment with Garcia Munoz (2007), the dissociation of H<sub>2</sub> is caused by dissocia-  
288 tion of H<sub>2</sub>O, which leads to the production of OH radicals that attack the H<sub>2</sub>  
289 molecules. We note that the exact location of the H<sub>2</sub>/H transition depends  
290 on the temperature profile and, depending on the thermal structure, it could  
291 occur even below the 1  $\mu$ bar level.

292 The major oxygen-bearing molecules, CO and H<sub>2</sub>O, have roughly equal  
293 abundances from 10 to 10<sup>-5</sup> bar. This is in line with thermochemical equi-  
294 librium at the temperatures and pressures relevant to HD209458b (Lodders  
295 and Fegley, 2002). H<sub>2</sub>O and CO are effectively dissociated at pressures lower  
296 than 0.3 and 0.1  $\mu$ bar, respectively. We note that molecular abundances  
297 could be significant at 0.1–1  $\mu$ bar, and technically the results of the hydro-  
298 dynamic calculations are only valid above the 0.1  $\mu$ bar level. The presence of  
299 molecules such as H<sub>2</sub>, H<sub>2</sub>O, and CO can lead to enhanced UV heating as well  
300 as efficient radiative cooling by H<sub>3</sub><sup>+</sup>, H<sub>2</sub>O and CO in the 0.1–1  $\mu$ bar region.

301 The photochemical model also includes the chemistry of silicon. Due



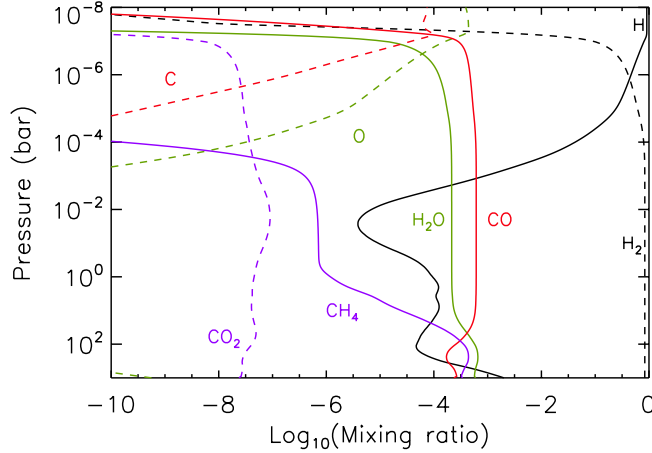


Figure 1: Mixing ratios of key oxygen and carbon-bearing species in the dayside atmosphere of HD209458b (Lavvas et al., *in preparation*).

302 to condensation into forsterite and enstatite (e.g Visscher et al., 2010), the  
 303 abundance of Si in the observable atmospheres of giant planets was thought to  
 304 be negligible and thus the photochemistry of silicon in planetary atmospheres  
 305 has not been studied before. The photochemical calculations indicate that,  
 306 in agreement with thermochemical calculations (Visscher et al., 2010), SiO  
 307 is the dominant silicon-bearing gas. SiO dissociates in the thermosphere at a  
 308 similar pressure level as H<sub>2</sub>O and CO. We note that the detection of Si<sup>2+</sup> in  
 309 the thermosphere implies that silicon does not condense in the atmosphere  
 310 of HD209458b (Paper II).

311 In addition to composition, lower boundary conditions are required for  
 312 temperature and velocity. We specified  $T_0$  and  $p_0$  at the lower boundary, and

313 used them to calculate  $\rho_0$  from the ideal gas law. The steady state continuity  
314 equation  $\rho_0 v_0 r^2 = F_c$ , where  $F_c$  is the flux constant, was used to calculate the  
315 velocity  $v_0$  at the lower boundary during each time step. The flux constant is  
316 solved self-consistently by the model, and it depends largely on the terms in  
317 the energy equation. In general we assumed that  $T_0 \approx 1,300$  K, which is close  
318 to the effective temperature of the planet. We note that this temperature  
319 is largely unconstrained. Radiative transfer models for close-in EGPs (e.g.,  
320 Showman et al., 2009, and references therein) do not account for heating by  
321 stellar UV radiation or possible opacity sources created by photochemistry  
322 (e.g., Zahnle et al., 2009). Therefore these models may not accurately predict  
323 the temperature at the base of the thermosphere.

324 Sing et al. (2008a,b) used observations of the Na D line profile to constrain  
325 the temperature profile in the upper atmosphere. They suggested that Na  
326 condenses into clouds near the 3 mbar level, and thus predicted a deep min-  
327 imum in temperature in this region that is required for condensation. The  
328 detection of  $\text{Si}^{2+}$  implies that condensation of Na in the lower atmosphere is  
329 unlikely (Paper II), and thus this result is unreliable. Relying on the same  
330 observations, Vidal-Madjar et al. (2011a,b) predicted that the temperature  
331 increases steeply from 1,300 K to 3,500 K near the 1  $\mu\text{bar}$  level. However,  
332 their method to retrieve the temperature relies on the density scale height  
333 of Na to express the optical depth along the line of sight (LOS). This is not  
334 consistent with the argument that Na is depleted above the 3 mbar level.  
335 If such a depletion takes place, the density scale height of Na is not the

336 same as the scale height of the atmosphere and it cannot be used to retrieve  
337 temperatures.

### 338 *2.1.2. Upper boundary conditions*

339 Previous models of the thermosphere disagree on the details of the density  
340 and temperature profiles (e.g., Yelle, 2004; Tian et al., 2005; Garcia Munoz,  
341 2007; Murray-Clay et al., 2009). This is partly due to different boundary con-  
342 ditions, although assumptions regarding the heating rates and composition  
343 are probably more important (see Section 3.1). Unfortunately, the planetary  
344 wind equations can have an infinite number of both subsonic and supersonic  
345 solutions. In time-dependent models, the upper boundary conditions in par-  
346 ticular can determine if the solution is subsonic or supersonic, and they can  
347 alter the temperature and velocity profiles (e.g., Garcia Munoz, 2007). The  
348 choice of proper boundary conditions is therefore important.

349 Volkov et al. (2011a,b) studied the escape of neutral atmospheres under  
350 different circumstances by using the kinetic Monte Carlo (DSMC) method.  
351 Because the fluid equations are a simplification of the kinetic equations at low  
352 values of  $Kn$ , the hydrodynamic model should ideally be consistent with the  
353 DSMC results both above and below the exobase. Volkov et al. (2011a,b)  
354 found that the nature of the solutions depends on the thermal escape pa-  
355 rameter  $X_0 = GM_p m / kT_0 r_0$  and the Knudsen number  $Kn_0$  at the lower  
356 boundary  $r_0$  of a region where diabatic heating is negligible. They argued  
357 that hydrodynamic escape is possible when  $X_0 < 2-3$  (see also Opik, 1963;

358 Hunten, 1973). When  $X_0 \gtrsim 3$ , on the other hand, the sonic point is at such  
359 a high altitude that the solution is practically subsonic and with  $X_0 \gtrsim 6$  the  
360 escape rate is similar to the thermal Jeans escape rate.

361 The results of the DSMC calculations can be incorporated into hydro-  
362 dynamic models with appropriate upper boundary conditions. Volkov et al.  
363 (2011a,b) suggest that the modified Jeans escape rate, which is based on the  
364 drifting Maxwellian velocity distribution function, is a good approximation  
365 of the DSMC results in fluid models, consistent with Yelle (2004). In order  
366 to contrast the modified Jeans upper boundary conditions (hereafter, the  
367 modified Jeans conditions) with other possibilities, we used them and the  
368 extrapolated upper boundary conditions (hereafter, the ‘outflow’ conditions)  
369 adopted by Tian et al. (2005) and Garcia Munoz (2007) in our simulations.  
370 In general, we placed the upper boundary at  $16 R_p$ . The impact of the  
371 boundary conditions is discussed in Section 3.1.5.

372 We formulated the outflow conditions simply by extrapolating values for  
373 density, temperature and velocity with a constant slope from below. For the  
374 modified Jeans conditions, we calculated the effusion velocity  $v_s$  at the upper  
375 boundary separately for each species by using equation (9) from Volkov et  
376 al. (2011b). Using this equation violates the conservation of electric charge  
377 at the upper boundary because the small mass of the electrons causes their  
378 velocity to be much larger than the velocity of the protons. In reality charge  
379 separation is prevented by the generation of an ambipolar electric field that  
380 ensures that the vertical current is zero at the upper boundary. This elec-

381 tric field causes the ions to escape faster while it slows the electrons down.  
 382 Effectively this lowers the escape velocity ( $v_{\text{esc}} = \sqrt{2GM/r}$ ) of the ions and  
 383 increases the escape velocity of the electrons.

384 In order to incorporate the ambipolar electric field in the modified Jeans  
 385 conditions we expressed the Jeans parameters for ions and electrons as:

$$X_i = \frac{GMm_i}{kTr} - \frac{\phi_e q_i}{kT} \quad (4)$$

$$X_e = \frac{GMm_e}{kTr} + \frac{\phi_e |q_e|}{kT} \quad (5)$$

386 where  $\phi_e$  is the ambipolar electric potential,  $q_{i,e}$  is the electric charge and  
 387 subscripts  $i$  and  $e$  stand for electrons and ions, respectively. We used these  
 388 Jeans parameters to calculate the effusion velocities for the electrons and ions,  
 389 and then solved iteratively for  $\phi_e$  by using the condition of zero current i.e.,  
 390  $n_e |q_e| v_e = \sum_i n_i q_i v_i$ . This approach is consistent with kinetic models for the  
 391 solar and polar winds (Lemaire and Scherer, 1971a,b). Having obtained the  
 392 correct effusion velocities for the charged and neutral species, we evaluated  
 393 the mass weighted outflow velocity from:

$$v = \frac{1}{\rho} \sum_s \rho_s v_s \quad (6)$$

394 and used this velocity as an upper boundary condition. The values of tem-  
 395 perature and density that are required for this calculation were extrapolated  
 396 from below. As the model approaches steady state, the solution approaches

397 a value of  $v$  at the upper boundary that is consistent with the modified Jeans  
398 velocity.

### 399 *2.1.3. Numerical methods*

400 We solved the equations of motion on a grid of 400–550 levels with in-  
401 creasing altitude spacing. The radius  $r_n$  from the center of the planet at level  
402  $n$  is thus given by a geometric series (e.g., Garcia Munoz, 2007):

$$r_n = r_1 + \sum_{i=1}^{n-1} f_c^i \delta z_0 \quad (7)$$

403 where  $r_1 = 1.08 R_p$ ,  $\delta z_0 = 10$  km, and  $f_c = 1.014$ . We solved the equations of  
404 motions in two parts, separating advection (Eulerian terms) from the other  
405 (Lagrangian) terms. The Lagrangian solution is performed first, and all vari-  
406 ables are updated before advection. We used the flux conservative van Leer  
407 scheme (e.g., van Leer, 1979) for advection, and the semi-implicit Crank-  
408 Nicholson scheme (e.g, Jacobson, 1999) to solve for viscosity and conduction  
409 in the momentum and energy equations, respectively. We employed a time  
410 step of 1 s in all of our calculations. Despite the sophisticated numerical  
411 apparatus, the model is still occasionally unstable, particularly in the early  
412 stages of new simulations. The primary source of the instabilities are pres-  
413 sure fluctuations (sound waves) that are not balanced by gravity. We used  
414 a two-step Shapiro filter (Shapiro, 1970) periodically to remove numerical  
415 instabilities. We assumed that a steady state has been reached once the flux  
416 constant  $F_c$  is constant with altitude and the flux of energy is approximately

417 conserved.

## 418 **3. Results**

### 419 *3.1. Temperature and velocity profiles*

420 In this section we constrain the range of mean temperatures and veloci-  
421 ties based on stellar heating in the thermosphere of HD209458b and similar  
422 close-in EGPs. We discuss the general dependency of the temperature and  
423 velocity profiles on the net heating efficiency and stellar flux, and relate this  
424 discussion to new temperature and velocity profiles for HD209458b that are  
425 based on realistic photoelectron heating efficiencies calculated specifically for  
426 close-in EGPs. This discussion is necessary because the temperature and  
427 velocity profiles from previous models of the upper atmosphere differ signif-  
428 icantly, and the differences affect the density profiles of the observed species  
429 (see Section 3.2). As an example, Figure 2 shows the temperature profiles  
430 based on several earlier models. In addition to boundary conditions, the dis-  
431 crepancies evident in this figure arise from different assumptions about the  
432 heating rates.

#### 433 *3.1.1. General dependency*

434 We note that the thermal structure in the upper atmospheres of the giant  
435 planets in the solar system is not very well understood despite modeling and  
436 observations that are far more extensive than those available for extrasolar  
437 planets (e.g., Yelle and Miller, 2004). It is therefore useful test the reaction

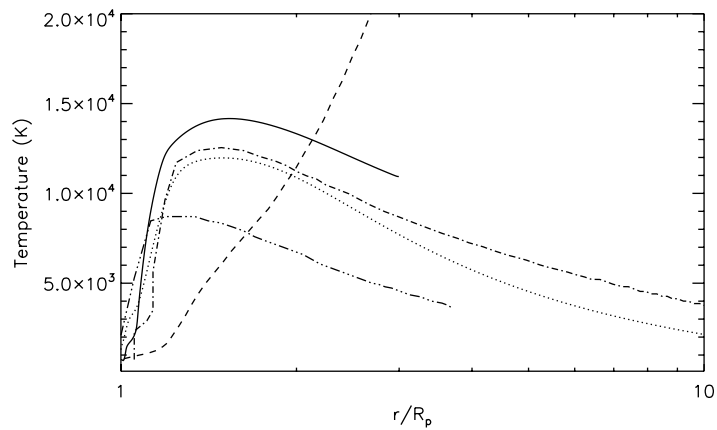


Figure 2: Some examples of temperature profiles from earlier models of the upper atmosphere of HD209458b. The solid line is from Figure 1 of Yelle (2004), the dotted line is from the C2 model in this work (see Section 3.1.2), the dashed line is the atomic hydrogen model from Figure 11 of Tian et al. (2005), the dashed-dotted line is the SP model from Figure 3 of Garcia Munoz (2007), and the dashed-triple-dotted line is from Figure 1 of Murray-Clay et al. (2009)



438 of the model to different heating rates and profiles. We used our model to  
439 calculate temperature and velocity profiles based on different heating efficien-  
440 cies and stellar fluxes. These profiles are shown in Figure 3. First, we used  
441 the average solar spectrum (Section 2.1) and varied the net heating efficiency  
442  $\eta_{\text{net}}$  from 0.1 to 1. Second, we multiplied the solar spectrum by factors of  
443 2x, 10x, and 100x, and used  $\eta_{\text{net}} = 0.5$ . The range of enhanced fluxes covers  
444 solar maximum conditions and stars that are more active than the sun. In  
445 each case we assumed that  $\eta_{\text{net}}$  is constant and does not vary with altitude.  
446 We used planetary parameters of HD209458b and set the upper boundary to  
447  $16 R_p$  with outflow boundary conditions, and the lower boundary to the 1  
448  $\mu\text{bar}$  level with a temperature of 1,300 K.

449 A net heating efficiency of 50 % is similar to the heating efficiency in  
450 the Jovian thermosphere (Waite et al., 1983), and we may consider this as  
451 a representative case of a typical gas giant (hereafter, the H50 model). The  
452 maximum temperature in the H50 model is 11,500 K and the temperature  
453 peak is located near  $1.5 R_p$  ( $p = 0.3 \text{ nbar}$ ). As  $\eta_{\text{net}}$  varies from 0.1 to 1, the  
454 peak shifts from  $1.4 R_p$  (0.5 nbar) to  $1.9 R_p$  (0.1 nbar) and the maximum  
455 temperature varies from 10,000 K to 13,200 K. It is interesting to note that  
456 the temperature profile depends strongly on the heating efficiency but the  
457 location of the peak and the maximum temperature depend only weakly on  
458  $\eta_{\text{net}}$ . This is because the vertical velocity increases with heating efficiency,  
459 leading to more efficient cooling by faster expansion that controls the peak  
460 temperature while enhanced advection and high altitude heating flatten the

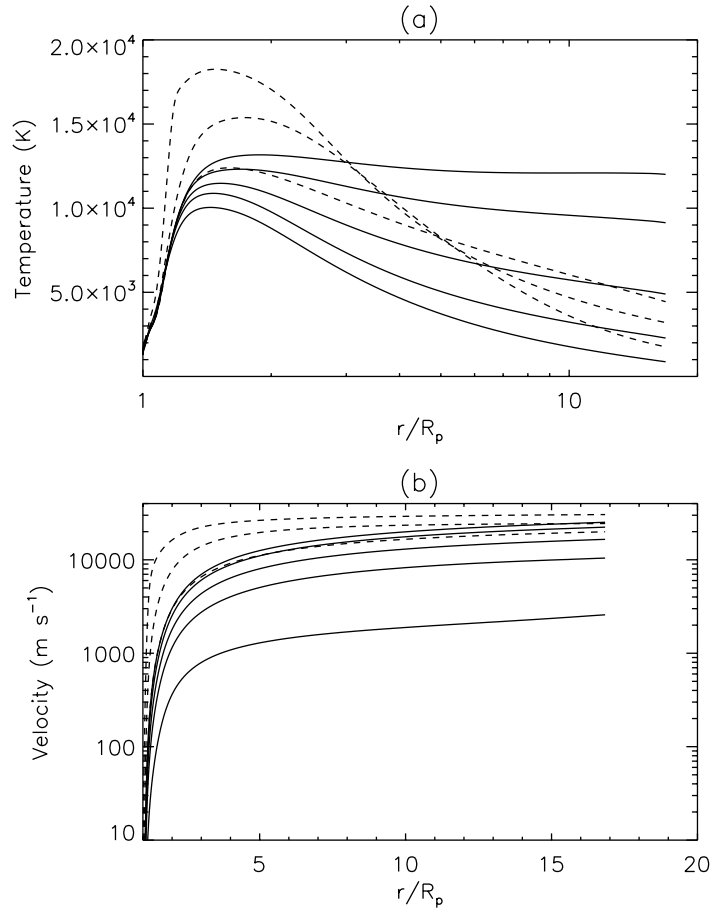


Figure 3: Temperature (a) and velocity (b) profiles in the upper atmosphere of HD209458b based on different heating efficiencies and stellar XUV fluxes. The solid lines show models based on the average solar flux with  $\eta_{\text{net}}$  of 0.1, 0.3, 0.5, 0.8, and 1 (from bottom to top). The dashed lines show models with  $\eta_{\text{net}} = 0.5$  and stellar flux of 2x, 10x, and 100x the solar average flux (in order of increasing peak temperature).

461 temperature gradient above the peak. As a result, the temperature profile is  
462 almost isothermal when  $\eta_{\text{net}} = 1$ .

463 It is also interesting that the temperature profiles in the models that are  
464 based on  $\eta_{\text{net}} = 0.5$  and the solar flux enhanced by factors of 2–100 differ  
465 from models with the average solar flux and a higher heating efficiency. For  
466 instance, one might naively assume that a model with  $\eta_{\text{net}} = 0.5$  and 2x the  
467 average solar flux would be similar to a model with the average solar flux  
468 and  $\eta_{\text{eta}} = 1$ . Suprisingly, this is not the case – despite the fact that the  
469 mass loss rates from these models are identical. This is because of the way  
470 radiation penetrates into the atmosphere – doubling the incoming flux is not  
471 the same as doubling the heating rate at each altitude for the same flux. As  
472 the stellar flux increases further, the temperature peak shifts first to higher  
473 altitudes, and then to lower altitudes so that for the 100x case the peak is  
474 located again near  $1.5 R_p$ . Despite the hugely increased stellar flux, the peak  
475 temperature is only 18,300 K for the 100x case. This is again because the  
476 enhanced adiabatic and advective cooling driven by faster expansion control  
477 the temperature even in the absence of efficient radiative cooling mechanisms.

478 Koskinen et al. (2010a) suggested that the mean temperature of the ther-  
479 mosphere below  $3 R_p$  can be constrained by observations, and used their  
480 empirical model to fit temperatures to the H Lyman  $\alpha$  transit data (Vidal-  
481 Madjar et al., 2003; Ben-Jaffel, 2007, 2008). A quantity that can be compared  
482 with their results is the pressure averaged temperature of the hydrodynamic

483 model, which is given by:

$$\overline{T}_p = \frac{\int_{p_1}^{p_2} T(p) d(\ln p)}{\ln(p_2/p_1)}. \quad (8)$$

484 For  $\eta_{\text{net}}$  ranging from 0.1 to 1, the pressure averaged temperature below  $3 R_p$   
485 varies from 6,200 K to 7,800 K for the average solar flux. In the H50 model  
486 the pressure averaged temperature is 7,000 K. We note that  $\overline{T}_p$  is a fairly  
487 stable feature of our solutions – in contrast to the details of the temperature  
488 profile and velocities it is relatively insensitive to different assumptions about  
489 the boundary conditions and heating efficiencies. Obviously,  $\overline{T}_p$  depends on  
490 the stellar flux, although it only increases to 9,800 K in the 100x case.

491 Koskinen et al. (2010a) inferred a mean temperature of 8,250 K in the  
492 thermosphere of HD209458b with  $p_0 = 1 \mu\text{bar}$  (the M7 model). Taken to-  
493 gether with our results based on solar XUV fluxes, this implies a relatively  
494 high heating efficiency. Alternatively, with  $\eta_{\text{net}} = 0.5$  it may imply that the  
495 XUV flux of HD209458b is 5–10 times higher than the corresponding solar  
496 flux. This type of an enhancement is not impossible. The activity level of  
497 the star depends on its rotation rate, and the rotation rate of HD209458 may  
498 be twice as fast as the rotation rate of the sun (Silva-Valio, 2008). However,  
499 the uncertainty of the observed H Lyman  $\alpha$  transit depths accommodates  
500 a range of temperatures, and thus we are unable to derive firm constraints  
501 on the heating rates from the observations. In general, though, the pressure  
502 averaged temperature provides a useful connection between observations and

503 temperatures predicted by models that can be exploited to constrain heating  
504 rates.

505 The effect of changing the heating efficiency on the velocity profile is  
506 quite dramatic. As  $\eta_{\text{net}}$  ranges from 0.1 to 1 (with the average solar flux),  
507 the velocity at the upper boundary increases from  $2.6 \text{ km s}^{-1}$  to  $25 \text{ km s}^{-1}$ .  
508 However, the velocity does not increase linearly with stellar flux or without  
509 a bound – in the 100x case the velocity at the upper boundary is only 30  
510  $\text{km s}^{-1}$ . An interesting qualitative feature of the solutions is that the sonic  
511 point moves to a lower altitude with increasing heating efficiency or stellar  
512 flux. With  $\eta_{\text{net}} = 0.1$  the isothermal sonic point is located above the upper  
513 boundary whereas with  $\eta_{\text{net}} = 1$  it is located at  $4 R_p$ . This behavior is re-  
514 lated to the temperature gradient and it is discussed further in Section 3.1.3.  
515 Basically the sonic point, when it exists, moves further from the planet as  
516 the high altitude heating rate decreases.

517 It is now clear that assumptions regarding the heating efficiency and ra-  
518 diative transfer have a large impact on the temperature and velocity profiles  
519 and the results from the previous models reflect this fact (see Figure 2). The  
520 differences between models have implications on the interpretation of obser-  
521 vations. For instance, Vidal-Madjar et al. (2003) and Linsky et al. (2010)  
522 suggested that the UV transit observations probe the velocity structure of  
523 the escaping gas. Obviously, the nature of this velocity structure depends  
524 on the properties of the upper atmosphere. On the other hand, Ben-Jaffel  
525 and Hosseini (2010) argued that the observations point to a presence of hot

526 energetic atoms and ions within the Roche lobe of the planet. We believe  
527 that it is important to properly quantify the role of stellar heating in creat-  
528 ing the hot, escaping material before other options are pursued. This means  
529 that detailed thermal structure calculations that rely on a proper descrip-  
530 tion of photoelectron heating efficiencies are required. Below we discuss a  
531 new approach to modeling the temperature profile in the thermosphere of  
532 HD209458b and its impact on the velocity and density profiles.

### 533 *3.1.2. Energy balance and temperatures on HD209458b*

534 In the previous section we discussed models where the net heating effi-  
535 ciency  $\eta_{\text{net}}$  was fixed at a constant value at all altitudes. In this section we  
536 discuss more realistic models of HD209458b that rely on new approximations  
537 of photoelectron heating efficiency and derive an estimate of  $\eta_{\text{net}}$  based on  
538 these models. Here we also include radiative cooling from recombination and,  
539 in one case, H Lyman  $\alpha$  emissions by excited H (Murray-Clay et al., 2009).  
540 Our aim was to calculate the most likely range of temperatures in the ther-  
541 mosphere of HD209458b based on average solar fluxes. Figure 4 shows the  
542 temperature and velocity profiles at 1–5  $R_p$  based on different approxima-  
543 tions (see Table 2 for the input parameters). Model C1 assumes a constant  
544 photoelectron heating efficiency of 93 % at all altitudes and photoelectron  
545 energies. This heating efficiency is appropriate for photoelectrons created by  
546 50 eV photons at an electron mixing ratio of  $x_e = 0.1$  (Cecchi-Pestellini et  
547 al., 2009). Model C2 is otherwise similar to C1 but the heating efficiency

548 varies with photoelectron energy and altitude (see below). Models C3 and  
 549 C4 are also based on C1, but C3 includes the substellar tidal forces in the  
 550 equations of motion (e.g., Garcia Munoz, 2007) and C4 includes Lyman  $\alpha$   
 551 cooling. All of these models are based on the outflow boundary conditions  
 552 for temperature, velocity, and density.

Table 2: Model input parameters and results

Model <sup>a</sup>	$r_\infty$ ( $R_p$ ) <sup>b</sup>	$\eta_{\text{net}}$ <sup>c,d</sup>	$\dot{M}$ ( $10^7$ kg s <sup>-1</sup> )	$\bar{T}_p$ (K) <sup>e</sup>
C1	16 E	0.56 C	5.6	7250
C2	16 E	0.44 V	4.0	7200
C3	16 E,T	0.57 C	6.4	6450
C4	16 E	0.46 C	4.5	7110
C5	36 J	0.56 C	5.6	7290
C6	16 J	0.45 V	3.9	7310

<sup>a</sup>All models assume  $p_0 = 10^{-6}$  bar and  $T_0 = 1,300$  K.

<sup>b</sup>E - Outflow conditions, J - Modified Jeans conditions, T - Substellar tide.

<sup>c</sup>Net heating efficiency (see Section 2.1) i.e., the ratio of the net heating flux at all wavelengths to the unattenuated stellar flux ( $0.45$  W m<sup>-2</sup>) at wavelengths shorter than  $912$  Å.

<sup>d</sup>C - Constant photoelectron heating efficiency, V - Varying photoelectron heating efficiency (see text).

<sup>e</sup>Pressure averaged temperature below  $3 R_p$ .

553 Cecchi-Pestellini et al. (2009) also estimated the heating efficiencies for  
 554 photoelectrons released by photons of energy  $E \gtrsim 50$  eV at different values  
 555 of the electron mixing ratio  $x_e$ . We used their heating efficiencies for  $x_e = 0.1$   
 556 in the C2 model. They parameterized their results in terms of the vertical  
 557 column density  $N_{\text{H}}$  of H. We fitted the heating efficiency as a function of  $N_{\text{H}}$   
 558 for 50 eV photons with a regular transmission function, and modified this

559 function accordingly for different cutoff altitudes and heating efficiencies of  
 560 photons with different energies [see Figures 3 and 4 of Cecchi-Pestellini et al.  
 561 (2009)]. We note that  $x_e \approx 0.1$  near the temperature peak of our models and  
 562 thus the results are appropriate for our purposes. However, they are only  
 563 applicable to photons with  $E \gtrsim 50$  eV. We used simple scaling to estimate  
 564 the heating efficiencies for low energy photons with  $E < 50$  eV.

565 As  $N_H$  increases, the heating efficiency for 50 eV photons saturates at 93  
 566 %. We assumed that the saturation heating efficiency for low energy photons  
 567 is also 93 %. In reality, this heating efficiency may be closer to 100 % but  
 568 the difference is small. In order to estimate the altitude dependence of the  
 569 heating efficiency, we note that the rate of energy deposition by Coulomb  
 570 collisions between photoelectrons of energy  $E_p$  and thermal electrons with a  
 571 temperature  $T$  can be estimated from:

$$-\frac{dF_E}{dr} = L(E_p, e)\Phi_{pe}n_e \quad [\text{eV cm}^{-3} \text{ s}^{-1}] \quad (9)$$

572 where  $F_E$  is the flux of energy,  $\Phi_{pe}$  is the photoelectron flux ( $\text{cm}^{-2} \text{ s}^{-1}$ ),  $n_e$   
 573 is the density of thermal electrons ( $\text{cm}^{-3}$ ) and

$$L(E_p, e) = \frac{3.37 \times 10^{-12}}{n_e^{0.03} E_p^{0.94}} \left( \frac{E_p - E_e}{E_p - 0.53E_e} \right)^{2.36} \quad [\text{eV cm}^2],$$

574 with  $E_e = 8.618 \times 10^{-5} T_e$  is the stopping power (Swartz et al., 1971)<sup>1</sup>.

---

<sup>1</sup>Due to a historical precedent, the units here are in cgs.



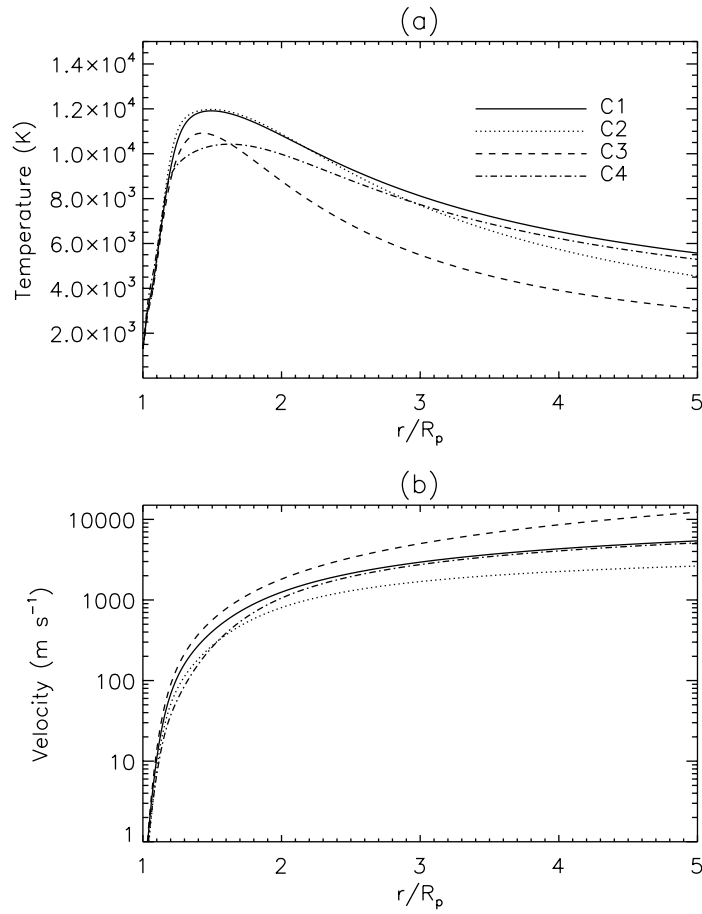


Figure 4: Temperature (a) and velocity (b) profiles in the upper atmosphere of HD209458b based on different models (see Table 2 for the input parameters).

575 Assuming that all of the energy is deposited by electrons that are thermalized  
 576 within a path element  $dr$ , we can estimate the e-folding length scale for  
 577 thermalization of photoelectrons with different energies as follows:

$$\Lambda_{pe} \approx \frac{E_p}{n_e L}. \quad (10)$$

578 We calculated  $\Lambda_{pe}$  for different photoelectrons based on the C1 model,  
 579 and compared the result with the vertical length scale  $H$  of the atmosphere.  
 580 The latter is either the scale height or  $R_p$ , depending on which is shorter.  
 581 When  $\Lambda_{pe}/H \gtrsim 0.005$ – $0.01$  we assumed that the heating efficiency decreases  
 582 with altitude according to the transmission function for 50 eV photons. The  
 583 limiting value was chosen to obtain a rough agreement with the results of  
 584 Cecchi-Pestellini et al. (2009) for 50 eV photons, and it implies that the  
 585 heating efficiency approaches zero when  $\Lambda_{pe}/H \gtrsim 0.1$ . We parameterized the  
 586 result in terms of the column density of H based on the density profiles of the  
 587 C1 model, and connected our results for low energy photoelectrons smoothly  
 588 with the results of Cecchi-Pestellini et al. (2009) for photons with  $E \gtrsim 50$  eV.  
 589 We then generated the C2 model from the C1 model with the new heating  
 590 efficiencies. Figure 5 shows the resulting heating efficiencies for 20, 30, 48,  
 591 and 100 eV photons.

592 Figure 6 shows the volume heating rate due to EUV photons of different  
 593 energies as a function of pressure based on the C2 model. The maximum  
 594 temperature of 12,000 K is reached near  $1.5 R_p$  ( $p = 0.6$  nbar). This re-

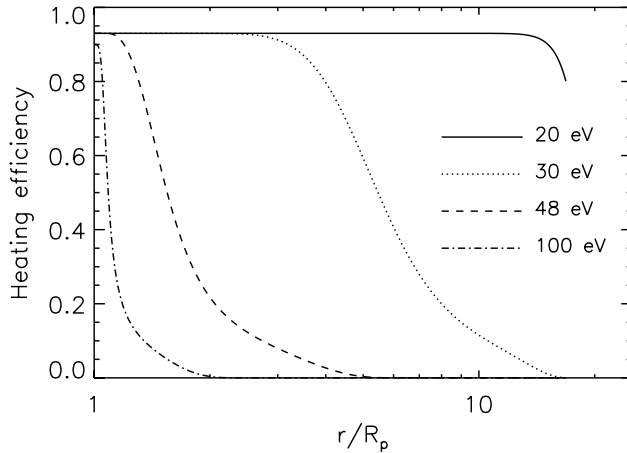


Figure 5: Heating efficiencies for photons of different energies (see text).

595 gion is heated mainly by EUV photons with wavelengths between 200 and  
 596 900 Å ( $E = 14\text{--}62$  eV). The saturation heating efficiency of 93 % for these  
 597 photons is higher than the corresponding heating efficiency in the Jovian  
 598 thermosphere (Waite et al., 1983). This is because of strong ionization that  
 599 leads to frequent Coulomb collisions between photoelectrons and thermal  
 600 electrons. Radiation with wavelengths shorter than 300 Å ( $E > 40$  eV) or  
 601 longer than 912 Å (13.6 eV) penetrates past the temperature peak to the  
 602 lower atmosphere. The heating efficiency for photons with  $E > 25$  eV ap-  
 603 proaches zero at high altitudes where heating is mostly due to low energy  
 604 EUV photons. The net heating efficiency for the C2 model is  $\eta_{\text{net}} = 0.44$   
 605 (Table 2), which is close to the H50 model. The location of the peak and  
 606 maximum temperature in the C2 model agree with the H50 model, but the

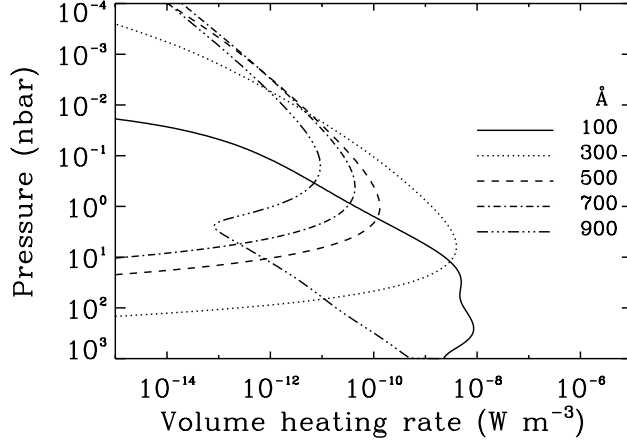


Figure 6: Volume heating rate as a function of pressure in the C2 model due to the absorption of stellar XUV radiation between 1 and 1000 Å in 200 Å bins.

607 temperature at higher altitudes in the C2 model decreases much more rapidly  
 608 with altitude than in the H50 model.

609 Figure 7 shows the terms in the energy equation based on the C2 model.  
 610 In line with previous studies, stellar heating is mainly balanced by adiabatic  
 611 cooling. Advection cools the atmosphere at low altitudes below the temper-  
 612 ature peak, whereas at higher altitudes it acts as a heating mechanism. In  
 613 fact, above  $2 R_p$  the adiabatic cooling rate is higher than the stellar heating  
 614 rate because thermal energy is transported to high altitudes by advection  
 615 from the temperature peak. The radiative cooling term that is centered near  
 616  $1.3 R_p$  arises from recombination following thermal ionization. Recombina-  
 617 tion following photoionization is included implicitly in the model and the rate

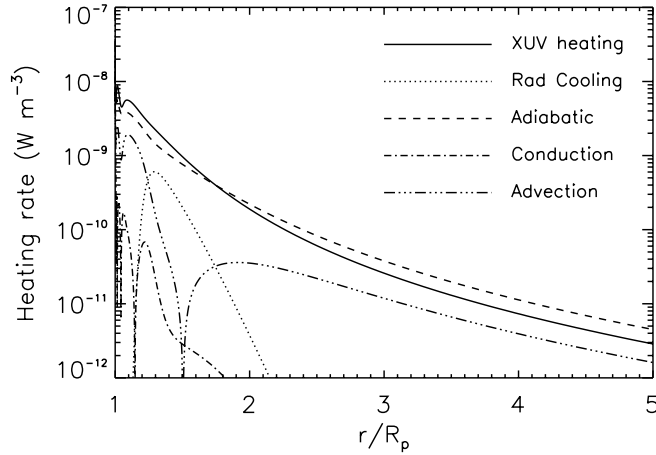


Figure 7: Volume heating rate based on the C2 model (absolute values). Advection acts as a cooling mechanism below  $1.5 R_p$  and a heating mechanism above this level.

618 is not included in the output. Conduction is not significant at any altitude  
 619 in the model. We note that the rates displayed in Figure 7 balance to high  
 620 accuracy, thus implying that the simulation has reached steady state.

621 The differences between the C1 and C2 models are subtle. The peak tem-  
 622 peratures are similar, and the temperature profiles generally coincide below  
 623  $3 R_p$ . Above this radius the temperature in the C2 model decreases more  
 624 rapidly with altitude than in the C1 model and subsequently the sonic point  
 625 moves to higher altitudes above the model domain. The results indicate that  
 626 the assumption of a constant photoelectron heating efficiency is appropriate  
 627 below  $3 R_p$  whereas at higher altitudes it changes the nature of the solu-  
 628 tion. This should not be confused with the assumption of a constant  $\eta_{\text{net}}$ ,

629 which leads to a different temperature profile when compared with either C1  
630 and C2 (see Figure 3). In general, the maximum and mean temperatures  
631 in models C1–C4 are relatively similar. Thus we conclude that the mean  
632 temperature in the thermosphere of HD209458b is approximately 7,000 K  
633 and the maximum temperature is 10,000–12,000 K.

634 The substellar tide is included in the C3 model. We included it mainly  
635 to compare our results with previous models (Garcia Munoz, 2007; Penz et  
636 al., 2008; Murray-Clay et al., 2009). The substellar tide is not a particu-  
637 larly good representation of the stellar tide in a globally averaged sense. In  
638 reality, including tides in the models is much more complicated than sim-  
639 ply considering the substellar tide (e.g., Trammell et al., 2011). Compared  
640 to the C1 model, the maximum temperature in the C3 model is cooler by  
641  $\sim 1,000$  K and at high altitudes the C3 model is cooler by 1,000–2,000 K.  
642 The velocity is faster and hence adiabatic cooling is also more efficient. The  
643 substellar tide drives supersonic escape (see also, Penz et al., 2008) and the  
644 sonic point in the C3 model is at a much lower altitude than in the C1 model  
645 (see Section 3.1.3). However, it is not clear how the sonic point behaves as a  
646 function of latitude and longitude. Given that the tide is also likely to induce  
647 horizontal flows, it cannot be included accurately in 1D models.

648 Murray-Clay et al. (2009) argued that radiative cooling due to the emis-  
649 sion of Lyman  $\alpha$  photons by excited H is important on close-in EGPs. The  
650 photons are emitted when the 2p level of H, which is populated by collisions  
651 with thermal electrons and other species, decays radiatively. We included

652 this cooling mechanism in the C4 model by using the rate coefficient from  
 653 Glover and Jappsen (2007) that includes a temperature-dependent correction  
 654 to the rate coefficient given by Black (1981). We also included an additional  
 655 correction factor of 0.1 based on detailed level population and radiative trans-  
 656 fer calculations by Menager et al. (2011). The effect of Lyman  $\alpha$  cooling is  
 657 largest near the temperature peak where the C4 model is 1,500 K cooler than  
 658 the C1 model, but generally the difference is not large. We note that the  
 659 H Lyman  $\alpha$  cooling rate here cannot be generalized as such to other EGPs  
 660 because the level populations and opacities depend on the thermal structure  
 661 and composition of the atmosphere.

### 662 3.1.3. Critical points

663 As we have pointed out, the location of the sonic point depends on the  
 664 energy equation through the temperature profile. Here we show that the use  
 665 of the isothermal approximation in estimating the location of the sonic point  
 666 can lead to significant errors unless the atmosphere really is isothermal. The  
 667 inviscid continuity and momentum equations can be combined to give an  
 668 expression for the critical point  $\xi_c$  of a steady-state solution (Parker, 1965):

$$-\frac{d}{d\xi} \left( \frac{c^2}{\xi^2} \right) = -\frac{1}{\xi^2} \frac{dc^2}{d\xi} + \frac{2c^2}{\xi^3} = \frac{W^2}{\xi^4} \quad (11)$$

669 where  $\xi = r/r_0$ ,  $c = \sqrt{kT/m}$  is the isothermal speed of sound,  $W = GM_p/r_0$ ,  
 670 and  $m$  is the mean atomic weight. It is often assumed that the vertical  
 671 velocity at the critical point is given by  $v^2 = c^2(\xi_c)$  so that the critical point

672 coincides with the isothermal sonic point (Parker, 1958). However, Parker  
673 (1965) suggested that subsonic solutions are also possible if the density at  
674 the base of the flow exceeds a critical value determined from the energy  
675 equation. In fact, he argued that conduction at the base of the corona may  
676 not be sufficient to drive a supersonic solar wind. This led him to suggest  
677 that supersonic expansion is possible only if there is significant heating of  
678 the corona over large distances above the base.

679 For an isothermal atmosphere with a temperature  $T_0$ , equation (11) re-  
680 duces to the famous result for the altitude of the sonic point (Parker, 1958):

681

$$\xi_c = \frac{W^2}{2c_0^2} \quad (12)$$

682 where  $W^2/c_0^2$  is the thermal escape parameter  $X_0$  at the lower boundary  
683  $r_0$ . The isothermal sonic point in the C1 model is located at  $7.2 R_p$  where  
684  $c(\xi_c) = 7.2 \text{ km s}^{-1}$ . The volume averaged temperature of the C1 model below  
685 this point is approximately 7,100 K. Assuming that  $r_0 = R_p$ ,  $T_0 = 7,100$   
686 K, and  $m = m_H$ ,  $X_0 \sim 16$  and equation (12) yields  $\xi_c \sim 8$ . In this case  
687 the analytic result agrees fairly well with the hydrodynamic model if one  
688 accounts for partial ionization of the atmosphere by assuming that the mean  
689 atomic weight<sup>2</sup> is  $m = 0.9 m_H$ .

690 On the other hand, the isothermal sonic point in the C2 model is at 15.4

---

<sup>2</sup>The mean atomic weight can be less than 1 because electrons contribute to the number density but not significantly to the mass density.



691  $R_p$  where  $c(\xi_c) = 4.1 \text{ km s}^{-1}$ . This is because the temperature gradient  
 692 of the model is steeper than the corresponding gradient in the C1 model.  
 693 The volume averaged mean temperature below  $15 R_p$  in the C2 model is  
 694 3,900 K. With this temperature and  $m = m_H$ , equation (12) predicts a  
 695 sonic point at  $14.6 R_p$ . However, at  $15 R_p$  the atmosphere is mostly ionized  
 696 and  $m = 0.6 m_H$ . With this value, the sonic point from equation (12)  
 697 would be located at  $8.8 R_p$ . These examples show that there are significant  
 698 caveats to using equation (12) to estimate the altitude of the sonic point on  
 699 close-in EGPs without accurate knowledge of the temperature and density  
 700 profiles. A variety of outcomes are possible and it is difficult to develop  
 701 a consistent criteria for choosing values of  $T$  and  $m$  that would produce  
 702 satisfactory results.

703 Another problem is that the atmosphere is not isothermal. In fact, the  
 704 temperature gradient above the heating peak in models C1–C4 (Table 2) is  
 705 relatively steep, and in some cases it approaches the static adiabatic gradient  
 706 ( $T \propto r^{-1}$ ) as defined by Chamberlain (1961). Assuming that the temperature  
 707 profile can be fitted with  $c^2 = c_0^2/\xi^\beta$  above the heating peak, the estimated  
 708 values of  $\beta$  for the C1 and C2 models are 0.7 and 0.9, respectively. We note  
 709 that the velocity in the C1 model exceeds the isentropic speed of sound ( $c_\gamma =$   
 710  $\sqrt{\gamma kT/m}$  where  $\gamma = 5/3$ ) at  $9.8 R_p$  where  $c_\gamma = 8.7 \text{ km s}^{-1}$ . This altitude  
 711 is significantly higher than the altitude of the isothermal sonic point. The  
 712 velocity in the C2 model does not exceed the isentropic speed of sound below  
 713 the upper boundary of  $16 R_p$ . Thus the temperature profile has a significant

714 impact on the nature of the solution and the escape mechanism. This means  
715 that estimating the altitude of the sonic point without observations and  
716 detailed models for guidance is almost certain to produce misleading results.

717 Past models for the upper atmosphere of HD209458b have predicted a  
718 variety of altitudes for the sonic point. On the other hand, Yelle (2004)  
719 pointed out that stellar heating in the thermosphere is mostly balanced by  
720 adiabatic cooling and our calculations confirm this. Parker (1965) argued  
721 that the critical point stretches to infinity when  $\beta \rightarrow 1$  i.e., as the temperature  
722 gradient is close to adiabatic. Based on this, we should perhaps expect that  
723 the sonic point on close-in EGPs is located at a fairly high altitude. This  
724 is confirmed by our hydrodynamic simulations. In all of our models except  
725 for one, the sonic point is located significantly above  $5 R_p$ . The exception  
726 is the C3 model, which includes the substellar tide. The isentropic sonic  
727 point in this model is located at  $3.9 R_p$  where  $c_\gamma = 8.2 \text{ km s}^{-1}$ . This is  
728 because the substellar tide leads to a lower effective value of the potential  
729  $W$ . However, the tidal potential depends on latitude and longitude, and the  
730 substellar results cannot be generalized globally.

#### 731 *3.1.4. Mass loss rates*

732 Here we evaluate the mass loss rates based on our models. We define the  
733 mass loss rate simply as:

$$\dot{M} = 4\pi r^2 \rho v. \quad (13)$$

734 We note that the solar spectrum that we used in this study contains the total  
 735 flux of  $4 \times 10^{-3} \text{ W m}^{-2}$  at wavelengths shorter than  $912 \text{ \AA}$  (the ionization  
 736 limit of H) when normalized to 1 AU. This value is close to the average solar  
 737 flux of  $3.9 \times 10^{-3} \text{ W m}^{-2}$  at the same wavelengths (e.g., Ribas et al., 2005).  
 738 In order to simulate a global average, we divided the flux by a factor of 4  
 739 in the model. This means that the incident flux on HD209458b at 0.047 AU  
 740 with wavelengths shorter than  $912 \text{ \AA}$  in our model is  $0.45 \text{ W m}^{-2}$ . The net  
 741 heating efficiencies given in Table 2 are based on this value.

742 Considering first the models with constant  $\eta_{\text{net}}$  ranging from 0.1 to 1 (see  
 743 Section 3.1.1), the mass loss rate varies almost linearly with  $\eta_{\text{net}}$  from  $10^7$   
 744  $\text{kg s}^{-1}$  and  $10^8 \text{ kg s}^{-1}$  while the pressure averaged temperature below  $3 R_p$   
 745 changes only by 1,500 K. This is because in a hydrodynamic model such  
 746 as ours the net energy has nowhere else to go but adiabatic expansion and  
 747 cooling, and thus escape is energy-limited. The bulk of the energy is absorbed  
 748 below  $3 R_p$ , and the mass loss rate is largely set by radiative transfer in this  
 749 region. The mass loss rate for HD209458b predicted by the C2 model is  
 750  $4.1 \times 10^7 \text{ kg s}^{-1}$  ( $\eta_{\text{net}} = 0.44$ ). The C3 model has the highest mass loss rate,  
 751 although this rate is only higher by a factor of 1.13 than the mass loss rate  
 752 in the C1 model. Thus we predict a mass loss rate of  $4\text{--}6 \times 10^7 \text{ kg s}^{-1}$  from  
 753 HD209458b based on the average solar flux at 0.047 AU.

754 Garcia Munoz (2007) demonstrated that the mass loss rate is insensitive  
 755 to the upper boundary conditions even when they have a large impact on  
 756 the temperature and velocity profiles, particularly at high altitudes. Indeed,

757 complex hydrodynamic models are not required to calculate mass loss rates  
758 under energy-limited escape as long as reasonable estimates of the net heating  
759 efficiency are available. It is also important to note that the current estimates  
760 of mass loss rates based on the observations (e.g., Vidal-Madjar et al., 2003)  
761 are not direct measurements. Instead, they are all based on different models.  
762 However, models that predict the same mass loss rate can predict different  
763 transit depths and models predicting different mass loss rates can match the  
764 observations equally well. Thus the models should not be judged on how well  
765 they agree with published mass loss rates but rather on how well they agree  
766 with the observed density profiles or transit depths. Hydrodynamic models  
767 with realistic heating rates are required to match the observations, and the  
768 mass loss rate then follows.

769 The globally averaged mass loss rate of about  $4\text{--}6 \times 10^7 \text{ kg s}^{-1}$  from  
770 HD209458b agrees well with similar estimates calculated by Yelle (2004,  
771 2006) and Garcia Munoz (2007), respectively, but it is significantly larger  
772 than the value calculated by Murray-Clay et al. (2009). These authors re-  
773 port a mass loss rate of  $3.3 \times 10^7 \text{ kg s}^{-1}$  based on the substellar atmosphere.  
774 When multiplied by 1/4 this corresponds to a global average rate of about  
775  $8.3 \times 10^6 \text{ kg s}^{-1}$ . However, the substellar mass loss rate is also enhanced by  
776 tides, so a comparable global average taking this into account would be even  
777 less than  $8.3 \times 10^6 \text{ kg s}^{-1}$ , which is already roughly a factor of 6 smaller than  
778 our calculations.

779 The Murray-Clay et al. (2009) models differ in many respects from the

780 models described here including the treatment of boundary conditions and  
781 radiative cooling, the numerical approach, and the adoption of a gray ap-  
782 proximation for stellar energy deposition. In order to explore the reason for  
783 the disagreement in escape rates, we have modified our model to implement  
784 the gray assumption by using the approach described in Murray-Clay et al.  
785 (2009) (see Section 3.2). Specifically, we adopted an incident flux<sup>3</sup> of 0.45  
786  $\text{W m}^{-2}$  and a mean photon energy of 20 eV. The mass loss rate based on the  
787 substellar atmosphere for this model is  $2.8 \times 10^7 \text{ kg s}^{-1}$ , in good agreement  
788 with the Murray-Clay et al. (2009) results. Thus, the difference between the  
789 Murray-Clay et al. (2009) models and the others is due to the gray assump-  
790 tion, and the fact that they estimated the incident flux on HD209458b based  
791 on the solar flux integrated between 13 eV and 40 eV. This energy range  
792 contains only about 25 % of the total solar flux at energies higher than 13.6  
793 eV.

794 Although not discussed by Murray-Clay et al. (2009), the restricted en-  
795 ergy range is likely an attempt to account for the fact that the absorption  
796 cross section decreases with energy implying that photons of sufficiently high  
797 energy will be absorbed too deep in the atmosphere to affect escape or the  
798 thermal structure, or composition of the thermosphere. Whether this is true,  
799 however, depends on the composition and temperature of the atmosphere.  
800 The gray assumption also fails to include the fact that the net heating effi-

---

<sup>3</sup>By chance the incident flux is equal to the mean solar flux divided by 4 that we used as a ‘globally averaged’ value. Here, however, it is taken to be the substellar value.

801 ciency increases with higher photon energy. These difficulties highlight the  
802 basic problem with a gray model, that the results can only be accepted with  
803 confidence if verified by a more sophisticated calculation or direct observa-  
804 tions.

### 805 *3.1.5. Constraints from kinetic theory*

806 Hydrodynamic models should be consistent with kinetic theory of rar-  
807 efied media even if the modeled region is below the exobase. This is because  
808 the atmosphere is escaping to space, and the density decreases with altitude,  
809 falling below the fluid regime at some altitude above the exobase. There-  
810 fore the conditions in the exosphere affect the flow solutions even below the  
811 exobase. Inappropriate use of the hydrodynamic equations can lead one to  
812 overestimate the flow velocity and mass loss rate, and these errors also affect  
813 the temperature and density profiles. Thus it is important to demonstrate  
814 that the hydrodynamic solutions agree with constraints from kinetic theory  
815 (e.g., Volkov et al., 2011a,b).

816 As an example, we calculated  $Kn_0$  and  $X_0$  (see Section 2.1.2) based on the  
817 C1 and C2 models. The Knudsen number  $Kn$  depends on the mean collision  
818 frequency, and it is much smaller than unity at all altitudes below  $16 R_p$ .  
819 Thus the exobase is located above the model domain (see also Murray-Clay  
820 et al., 2009). Calculating values for  $X_0$  is complicated by the broad stellar  
821 heating profile. We consider the region where stellar heating is negligible to

822 be where the flux of energy

$$E_\infty = F_c \left( c_p T + \frac{1}{2} v^2 - \frac{GM_p}{r} \right) - \kappa r^2 \frac{\partial T}{\partial r} \quad (14)$$

823 is approximately constant. This criteria is consistent with the equations of  
824 motion, and it means that  $r_0$  that should be used to calculate  $X_0$  is above  
825 the upper boundary of our model because significant stellar heating persists  
826 at all altitudes. Thus we evaluated values of  $X$  near the upper boundary for  
827 guidance. We also calculated the values with both the mass of the proton  
828 ( $X_H$ ) and the mean atomic weight ( $X$ ).

829 In the C1 model,  $X_H$  decreases with altitude, and above  $11.4 R_p$  it has  
830 values of less than 3. The mean atomic weight near the upper boundary is  
831  $\sim 0.6$  amu, and thus the general value of  $X < 2$  above  $11.1 R_p$ . The sonic  
832 point in the C1 model is below  $11 R_p$ , and it is in a region where stellar  
833 heating is significant. In the C2 model, both  $X$  and  $X_H$  are greater than 3  
834 at all altitudes below  $16 R_p$ . In fact,  $X$  increases with altitude above  $9 R_p$   
835 because the temperature gradient parameter exceeds unity. Thus the values  
836  $X$  in the C1 and C2 models are consistent with the difference in altitude  
837 between the sonic points in these models (see Section 3.1.3). Indeed, our  
838 results show, in line with Parker's original ideas about the solar wind, that  
839 supersonic escape is possible if there is significant heating of the atmosphere  
840 over large distances above the temperature peak. Such heating flattens the  
841 temperature gradient and brings the sonic point closer to the planet.

842 We note that there are some caveats to applying the simple criteria based  
843 on  $Kn_0$  and  $X_0$  to close-in extrasolar planets. The upper atmospheres of  
844 these planets are strongly ionized, and the DSMC simulations of Volkov et  
845 al. (2011a,b) apply only to neutral atmospheres. Partly due to ionization,  
846 the collision frequencies in the thermospheres of close-in planets are also  
847 high. Further, the atmospheres are affected by a broad stellar heating pro-  
848 file in altitude whereas the DSMC calculations do not include any diabatic  
849 heating. However, the results of Volkov et al. (2011a,b) also indicate that  
850 consistency with kinetic theory can be enforced approximately by applying  
851 the modified Jeans conditions to the hydrodynamic model at some altitude  
852 close to the exobase. This result is likely to be more general, and it applies  
853 to ionized atmospheres as long as ambipolar diffusion is taken into account  
854 (see Section 2.1.2).

855 We compared the temperature and velocity profiles from the C1 and C2  
856 models with results from similar models C5 and C6 that use the modified  
857 Jeans conditions. Note again that our version of the modified Jeans condi-  
858 tions includes the polarization electrostatic field that is required in strongly  
859 ionized media. Figure 8 shows the temperature and velocity profiles from the  
860 models. There is no difference between the C5 model and the C1 model as  
861 long as the upper boundary of the C5 model is at a sufficiently high altitude.  
862 In this case we extended it to  $36 R_p$ . When the upper boundary is placed at  
863 lower altitudes, the flow decelerates and the temperature increases near the  
864 upper boundary. A comparison between the C2 and C6 models provides an



865 example of the difference that can arise when the modified Jeans boundary  
866 conditions are used significantly below the exobase. A better agreement is  
867 achieved if the upper boundary of the C6 model is placed at a slightly higher  
868 altitude. In summary, we have shown that the C1 and C2 models are both  
869 consistent with kinetic theory.

870 We note that extending the models to  $16 R_p$  or higher is not necessarily  
871 justified because it ignores the complications arising from the possible influ-  
872 ence of the stellar tide, the stellar wind, and interactions of the flow with the  
873 magnetic field of the planet or the star. We placed the upper boundary at  
874 a relatively high altitude to make sure that the boundary is well above the  
875 region of interest, but generally we do not consider our results to be accurate  
876 above  $3\text{--}5 R_p$ . Instead, our results provide robust lower boundary conditions  
877 for multidimensional models of the escaping material outside the Roche lobe  
878 of the planet. Such models often cannot include detailed photochemical or  
879 thermal structure calculations. The results from the more complex models  
880 can then be used to constrain the upper boundary conditions in 1D models.  
881 This type of an iteration is a complex undertaking, and it will be pursued in  
882 future work.

### 883 *3.2. Density profiles*

884 In this section we provide a qualitative understanding of the density pro-  
885 files and transition altitudes that affect the interpretation of the observations.  
886 Based on the gas giants in the solar system it might be expected that heavy

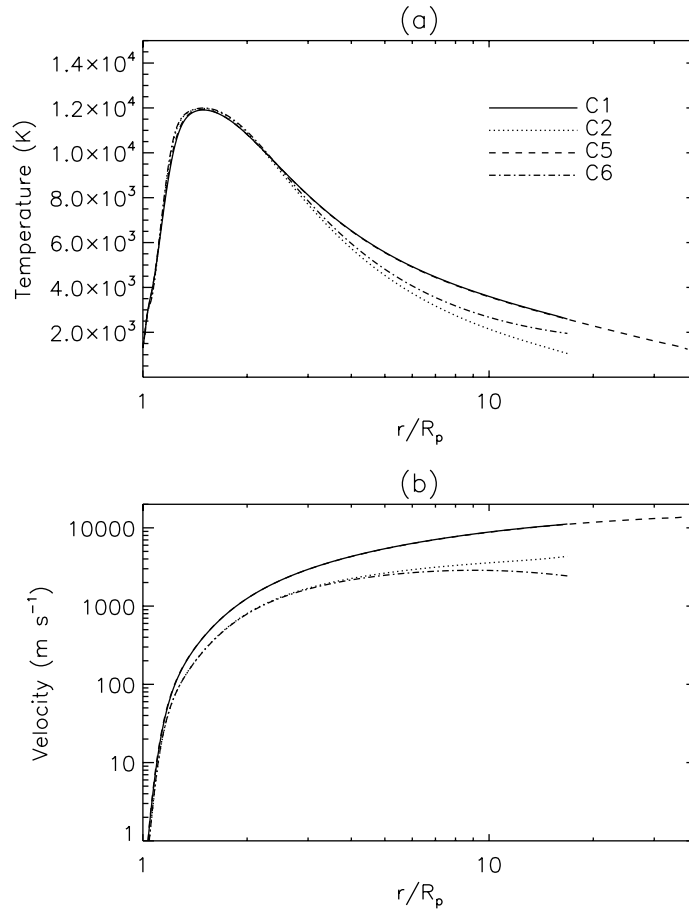


Figure 8: Temperature (a) and velocity (b) profiles in the upper atmosphere of HD209458b based on models with extrapolated and modified Jeans upper boundary conditions (see Table 2 for the input parameters).

887 species undergo diffusive separation in the thermosphere. If this were the  
888 case, the transit depths in the O I, C II, and Si III lines (Vidal-Madjar et al.,  
889 2004; Linsky et al., 2010) should not be significantly higher than the transit  
890 depth at visible wavelengths. It is therefore important to explain why diffu-  
891 sive separation does not take place in the thermosphere of HD209458b, and  
892 to clarify why H and O remain mostly neutral while C and Si are mostly ion-  
893 ized. Also, doubly ionized species such as  $\text{Si}^{2+}$  are not common in planetary  
894 ionospheres, and their presence needs to be explained. In order to do this,  
895 we modeled the ionization and photochemistry of the relevant species, and  
896 prove that diffusive separation does not take place.

897 In order to illustrate the results, Figure 9 shows the density profiles of  
898 H,  $\text{H}^+$ , He,  $\text{He}^+$ , O,  $\text{O}^+$ , C,  $\text{C}^+$ , Si,  $\text{Si}^+$ , and  $\text{Si}^{2+}$  from the C2 model. The  
899 location of the H/ $\text{H}^+$  transition obviously depends on photochemistry, but it  
900 also depends on the dynamics of escape. With a fixed pressure at the lower  
901 boundary, a faster velocity leads to a transition at a higher altitude. Thus  
902 the transition occurs near  $3.1 R_p$  in the C2 model whereas in the C1 and C3  
903 models it occurs at  $3.8 R_p$  and  $5 R_p$ , respectively. These results disagree with  
904 Yelle (2004) and Murray-Clay et al. (2009) who predicted a lower transition  
905 altitude, but they agree qualitatively with the solar composition model of  
906 Garcia Munoz (2007). They also agree with the empirical constraints derived  
907 by Koskinen et al. (2010a) from the observations.

908 Once again, the differences between the earlier models and our work arise  
909 from different boundary conditions, and assumptions regarding heating rates

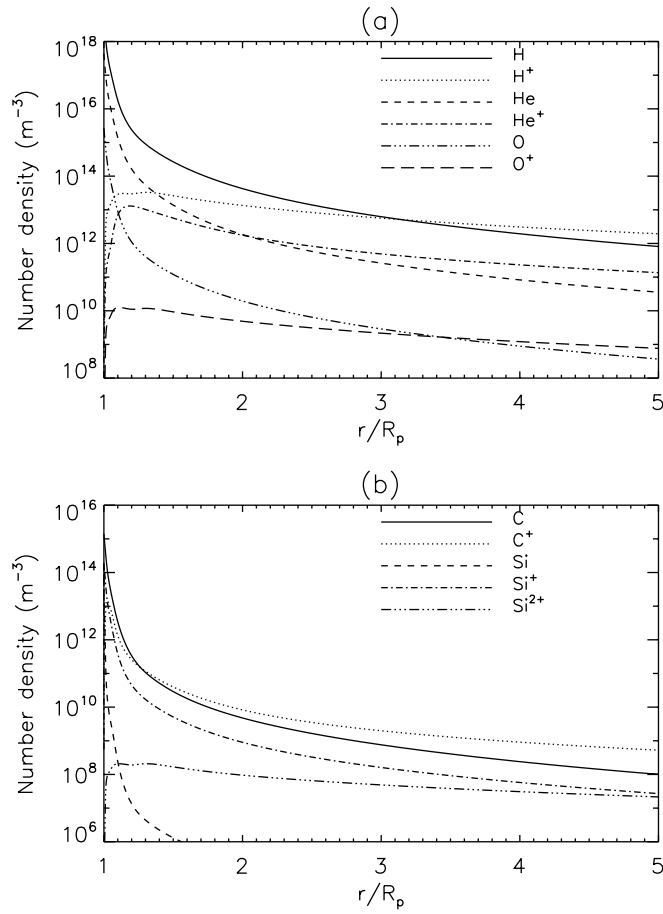


Figure 9: Density profiles in the upper atmosphere of HD209458b based on the C2 model (see Table 2 for the input parameters).

910 and photochemistry. We demonstrate this by reproducing the results of  
911 Murray-Clay et al. (2009) with our model. In order to do so, we set the  
912 lower boundary to 30 nbar with a temperature of 1,000 K, and included  
913 the substellar tide in the equations of motion. We only included H, H<sup>+</sup>,  
914 and electrons in the model, and used the recombination rate coefficient and  
915 Lyman  $\alpha$  cooling rate from Murray-Clay et al. (2009). We also calculated  
916 the heating and ionization rates with the gray approximation by assuming a  
917 single photon energy of 20 eV for the stellar flux of 0.45 W m<sup>-2</sup> at the orbital  
918 position of HD209458b. Figure 10 shows the density profiles of H and H<sup>+</sup>  
919 based on this model (hereafter, the MC09 model).

920 The H/H<sup>+</sup> transition in the MC09 model occurs near 1.4  $R_p$ . If we re-  
921 place the gray approximation with the full solar spectrum in this model, the  
922 H/H<sup>+</sup> transition moves higher to 2–3  $R_p$ . This is because photons with dif-  
923 ferent energies penetrate to different depths in the atmosphere, extending  
924 the heating profile in altitude around the heating peak. This is why the tem-  
925 perature at the 30 nbar level in the C2 model is 3,800 K and not 1,000 K.  
926 In order to test the effect of higher temperatures in the lower thermosphere,  
927 we extended the MC09 model to  $p_0 = 1 \mu\text{bar}$  (with  $T_0 = 1,300 \text{ K}$ ) and again  
928 used the full solar spectrum for heating and ionization. With these condi-  
929 tions, the H/H<sup>+</sup> transition moves up to 3.4  $R_p$ , in agreement with the C2  
930 model. We conclude that the unrealistic boundary conditions and the gray  
931 approximation adopted by Murray-Clay et al. (2009) and Guo (2011) lead  
932 to an underestimated overall density of H and an overestimated ion fraction.

933 Thus their density profiles yield a H Lyman  $\alpha$  transit depth of the order of  
934 2–3 % i.e., not significantly higher than the visible transit depth.

935 We note that Yelle (2004) also predicted a relatively low altitude of 1.7  
936  $R_p$  for the H/H<sup>+</sup> transition – despite the fact that his model does not rely on  
937 the gray approximation and the lower boundary is in the deep atmosphere.  
938 The reason for the low altitude of the H/H<sup>+</sup> transition in this case is the  
939 neglect of heavy elements. In the absence of heavy elements, H<sub>3</sub><sup>+</sup> forms near  
940 the base of the model and subsequent infrared cooling balances the EUV  
941 heating rates. This prevents the dissociation of H<sub>2</sub> below the 10 nbar level.  
942 In reality, reactions with OH and thermal decomposition dissociate H<sub>2</sub> near  
943 the 1  $\mu$ bar level (see Section 2.1.1) and cooling by H<sub>3</sub><sup>+</sup> is negligible at all  
944 altitudes. It should be noted that even if H<sub>2</sub> does not initially dissociate, H<sub>3</sub><sup>+</sup>  
945 can be removed from the lower thermosphere in reactions with carbon and  
946 oxygen species (e.g., Garcia Munoz, 2007) unless these species undergo diffu-  
947 sive separation. The subsequent lack of radiative cooling will then dissociate  
948 H<sub>2</sub> again near the 1  $\mu$ bar level.

949 In our models, charge exchange with oxygen (reactions R14 and R15 in  
950 Table 1) dominates the photochemistry of H below 3  $R_p$  and charge exchange  
951 with silicon (R25, R26) is also important below 1.4  $R_p$ . These reactions are  
952 secondary in a sense that they require the ions to be produced by some other  
953 mechanism. In fact, H<sup>+</sup> is mainly produced by photoionization (P1), al-  
954 though thermal ionization (R3) is also important near the temperature peak.  
955 The production rates are mainly balanced by loss to radiative recombination

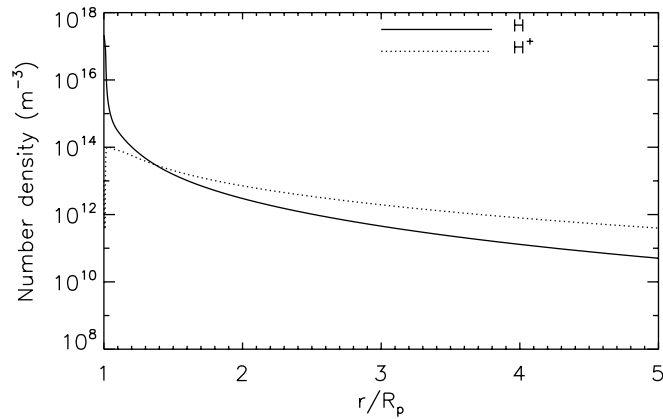


Figure 10: Density profiles of H and H<sup>+</sup> based on the MC09 model that is similar to that of Murray-Clay et al. (2009) (see text). Compared with our models (see Figure 9), the H/H<sup>+</sup> transition occurs at a significantly lower altitude. The difference arises from the lower boundary conditions and gray approximation to heating and ionization in the MC09 model.

956 (R1). The net chemical loss timescale for H is longer than the timescale for  
957 advection above  $1.7 R_p$ . This allows advection from below to replenish H at  
958 higher altitudes.

959 The density profiles of O and  $O^+$  are strongly coupled to H and  $H^+$   
960 by charge exchange (see also Garcia Munoz, 2007). As a result, the  $O/O^+$   
961 transition occurs generally near the  $H/H^+$  transition. For instance, in the  
962 C2 model it is located near  $3.4 R_p$ . The same is not true of carbon. The  
963  $C/C^+$  transition occurs at a much lower altitude than the  $H/H^+$  and  $O/O^+$   
964 transitions. For instance, in the C2 model it is located near  $1.2 R_p$ .  $C^+$  is  
965 mainly produced by photoionization (P4), although thermal ionization (R8)  
966 and charge exchange with  $He^+$  (R13) are also important near the temperature  
967 peak. The production is balanced by loss to radiative recombination (R10).  
968 The chemical loss timescale for C is shorter than the timescale for advection  
969 below  $1.8 R_p$ . Thus advection is unable to move the  $C/C^+$  transition to  
970 altitudes higher than  $1.2 R_p$ .

971 Silicon is almost fully ionized near the lower boundary of the model. Much  
972 of the  $Si^+$  below  $4 R_p$  is produced by charge exchange of Si with  $H^+$ ,  $He^+$ , and  
973  $C^+$  (R22, R23, R24). The low ionization potential of Si (8.2 eV) means that  
974  $Si^+$  can also be produced by thermal ionization (R18), and photoionization  
975 (P6) by stellar FUV radiation and X-rays that propagate past the EUV  
976 heating peak. Above  $4 R_p$ ,  $Si^+$  is mostly produced by photoionization. Linsky  
977 et al. (2010) suggested that the balance of  $Si^+$  and  $Si^{2+}$  depends on charge  
978 exchange with  $H^+$  and H, respectively, and our results confirm this. However,



979 the location of the  $\text{Si}^+/\text{Si}^{2+}$  transition also depends on the dynamics. For  
980 instance, in the C2 model it occurs near  $5.8 R_p$  while in the C1 model it  
981 occurs near  $8.5 R_p$ . Thus slow outflow and high temperatures favor  $\text{Si}^{2+}$  as  
982 the dominant silicon species as long as the flux constant is high enough to  
983 overcome diffusive separation (Paper II).

984 We have now explained the presence of the atoms and ions that have been  
985 detected in the thermosphere of HD209458b. Due to advection and charge  
986 exchange, H and O are predominantly neutral up to about  $3 R_p$  and give rise  
987 to the observed transit depths in the H Lyman  $\alpha$  and O I lines. Carbon, on  
988 the other hand, is ionized at a low altitude and thus  $\text{C}^+$  is also detectable in  
989 the upper atmosphere.  $\text{Si}^+$  is the dominant silicon species below  $5 R_p$ , but  
990 charge exchange with H ensures that there is also a significant abundance of  
991  $\text{Si}^{2+}$  in the atmosphere. We note that these conclusions are only valid if the  
992 heavier species are carried along to high altitudes by the escaping hydrogen.  
993 We show that this is the case below in Section 3.2.2.

### 994 *3.2.1. The EUV ionization peak (EIP) layer*

995 Koskinen et al. (2010b) explored the properties of the ionospheres of  
996 EGPs at different orbital distances from a Sun-like host star by using a hy-  
997 drostatic general circulation model (GCM) that also includes realistic heat-  
998 ing rates, photochemistry, and transport of constituents. They predicted  
999 that the EIP layer on HD209458b is centered at  $1.35 R_p$  where the electron  
1000 density is  $n_e = 6.4 \times 10^{13} \text{ m}^{-3}$  and  $x_e \sim 3 \times 10^{-2}$ . In the C2 model, the

1001 EIP layer is centered at  $1.3 R_p$  ( $p = 2$  nbar) where  $n_e = 4.4 \times 10^{13} \text{ m}^{-3}$  and  
1002  $x_e = 3.7 \times 10^{-2}$ . The vertical outflow velocity at  $1.3 R_p$  is  $90 \text{ m s}^{-1}$ . Thus  
1003 the results of Koskinen et al. (2010b) were not significantly affected by the  
1004 simplifying assumptions of the GCM. This means that hydrostatic GCMs  
1005 can be extended to relatively low pressures as long as the escape rates are  
1006 incorporated as boundary conditions.

1007 We also calculated the plasma frequency based on the electron densities  
1008 in the C2 model. This constrains the propagation of possible radio emissions  
1009 from the ionosphere. The ordinary plasma frequency  $\omega_p/2\pi$  exceeds 12 MHz  
1010 at all altitudes below  $5 R_p$  and reaches a maximum of almost 64 MHz in  
1011 the EIP layer. This presents a limitation on the detection of radio emissions  
1012 from the ionospheres of close-in EGPs. Any emissions that originate from  
1013 the ionosphere at  $1\text{--}5 R_p$  and have frequencies lower than  $10\text{--}70$  MHz can  
1014 be screened out by the ionosphere itself. We note that a detection of radio  
1015 emissions from an EGP has not yet been achieved (e.g., Bastian et al., 2000;  
1016 Lazio et al., 2007; Lecavelier des Etangs et al., 2011; Grießmeier et al., 2011).  
1017 Such a detection would be an important constraint on the magnetic field  
1018 strength and the ionization state of the source region (e.g., Grießmeier et al.,  
1019 2007). Models of the ionosphere are required to predict radio emissions from  
1020 the possible targets.

1021 *3.2.2. The escape of heavy atoms and ions*

1022 In this section we verify *a posteriori* that the velocity and temperature  
1023 differences between different species in the thermosphere of HD209458b are  
1024 small. This demonstrates that the single fluid approximation of the mo-  
1025 mentum and energy equations is valid, and that diffusive separation of the  
1026 heavy species does not take place. Our model includes velocity differences  
1027 between different species by including all of the relevant collisions between  
1028 them through the inclusion of diffusive fluxes in the continuity equations.  
1029 However, we have explicitly assumed that  $T_n = T_i = T_e$ , and this assumption  
1030 in particular needs to be verified. Also, the diffusion approach to the con-  
1031 tinuity equation is only valid if the velocity differences between the species  
1032 are reasonably small.

1033 We calculated the collision frequencies based on the C2 model, and found  
1034 that collisions with neutral H dominate the transport of heavy neutral atoms  
1035 such as O below  $3.5 R_p$ . At altitudes higher than this, collisions with  $H^+$  are  
1036 more frequent. In Paper II we demonstrate that a mass loss rate of  $6 \times 10^6$   
1037  $\text{kg s}^{-1}$  is required to prevent diffusive separation of O (the heaviest neutral  
1038 species detected so far) in the thermosphere. The mass loss rate in our mod-  
1039 els is  $\dot{M} > 10^7 \text{ kg s}^{-1}$  and thus O is dragged along to high altitudes by H. On  
1040 the other hand, collisions with  $H^+$  dominate the transport of heavy ions such  
1041 as  $\text{Si}^+$  as long as the ratio  $[\text{H}^+]/[\text{H}] \gtrsim 10^{-4}$  (Paper II). This explains why  
1042 Coulomb collisions in our models are more frequent than heavy ion-H colli-  
1043 sions at almost all altitudes apart from the immediate vicinity of the lower

1044 boundary. These collisions are much more efficient in preventing diffusive  
1045 separation than collisions with neutral H.

1046 Figure 11 compares the timescale for diffusion  $\tau_D$  for O and Si<sup>+</sup> with the  
1047 timescale for advection  $\tau_v$  based on the C2 model. In both cases,  $\tau_D \gg \tau_v$   
1048 and thus diffusion is not significant. This implies that there are no signifi-  
1049 cant velocity differences between heavy atoms and hydrogen. We note that  
1050 Coulomb collisions of doubly ionized species with H<sup>+</sup> are more frequent than  
1051 collisions between a singly ionized species and H<sup>+</sup>. Thus diffusion is even  
1052 less significant for a species like Si<sup>2+</sup>. We verified these results from our sim-  
1053 ulations by switching diffusion off in the model and rerunning the C2 model.  
1054 As a result the density of the heavy atoms and ions increased slightly at high  
1055 altitudes, but the differences are not significant – the results were nearly  
1056 identical to the density profiles of the original simulation.

1057 We note that the atmosphere can also be mixed by vertical motions asso-  
1058 ciated with circulation that are sometimes parameterized in one-dimensional  
1059 models by the eddy diffusion coefficient  $K_{zz}$  (e.g., Moses et al., 2011). This  
1060 mechanism is efficient in bringing the heavy elements to the lower thermo-  
1061 sphere but it is unlikely to mix the atmosphere up to  $3 R_p$  and beyond. Also,  
1062 there is no generally accepted method of estimating the degree of global mix-  
1063 ing based on circulation models, and most circulation models for EGPs do  
1064 not adequately treat the relevant energy deposition and forcing mechanisms  
1065 in the upper atmosphere. Thus there is considerable uncertainty over the val-  
1066 ues of  $K_{zz}$  and rapid escape is a much more likely explanation for the lack of

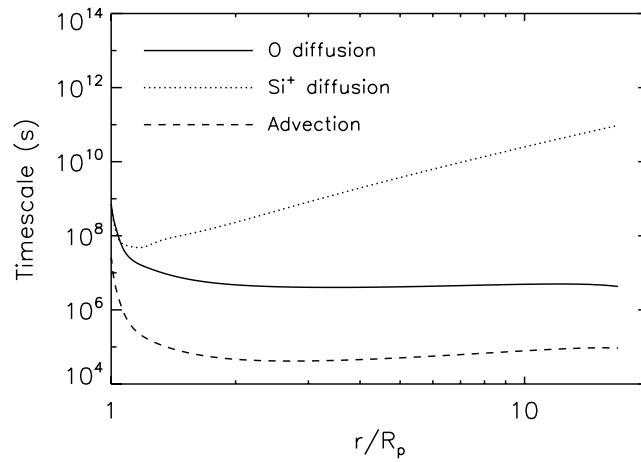


Figure 11: Timescales for diffusion  $\tau_D = H^2/D_s$  of O and Si<sup>+</sup>, and for advection  $\tau_v = H/v$  based on the C2 model. We calculated the diffusion coefficients in a mixture of H and H<sup>+</sup>. The large scale height of the atmosphere and relatively high collision frequencies mean that diffusion is not significant ( $\tau_D/\tau_v = vH/D_s \gg 1$ ) in the thermosphere of HD209458b.

1067 diffusive separation on HD209458b. In fact, the calculations of Koskinen et  
 1068 al. (2007b) show that the temperature in the thermosphere of planets such  
 1069 as HD209458b is high enough to practically guarantee an effective escape  
 1070 rate. The only way to prevent this is to provide enough radiative cooling to  
 1071 offset most of the XUV flux, but there are no radiative cooling mechanisms  
 1072 efficient enough to achieve this in a thermosphere composed of atoms and  
 1073 ions.

1074 As we noted above, the temperatures of the electrons, ions, and neutrals  
 1075 are roughly equal in the thermosphere of HD209458b. In order to show this,  
 1076 we assumed that photoelectrons share their energy with thermal electrons,  
 1077 which then share this energy further with ions and neutrals. We also as-  
 1078 sumed that the collisions frequencies between the species are higher than  
 1079 the timescale for advection. If the velocity differences between the species  
 1080 are negligible, the steady state 5-moment energy equations for thermal elec-  
 1081 trons and ions (Schunk and Nagy, 2000) can be used to obtain the following  
 1082 approximations<sup>4</sup>:

$$T_e - T_i \approx \frac{1}{3} \frac{m_i}{m_e} \frac{q_R}{kn_e \nu_{ei}} \quad (15)$$

$$T_i - T_n \approx \frac{1}{3} \frac{m_i + m_n}{m_i} \frac{q_R}{kn_i \nu_{in}} \quad (16)$$

1083 where  $q_R$  is the volume heating rate, and  $\nu_{ei}$  and  $\nu_{in}$  are the electron-ion and

---

<sup>4</sup>Note that conduction and viscosity are not important in the thermosphere of HD209458b.

1084 ion-neutral momentum transfer collision frequencies, respectively.

1085 We calculated the temperature differences for H, H<sup>+</sup>, and electrons based  
1086 on the C2 model. The difference between the electron and ion temperatures  
1087 decreases with altitude and is mostly less than 2 K. The difference between  
1088 the ion and neutral temperatures, on the other hand, increases with altitude.  
1089 The ion temperature is approximately 10 K higher than the neutral temper-  
1090 ature near 5  $R_p$  and the difference reaches 150 K at 16  $R_p$ . In both cases, the  
1091 temperature differences are negligible compared to the temperature of the  
1092 thermosphere. Further, the timescale for advection in the C2 model is al-  
1093 ways significantly longer than the relevant collision timescales. Thus we have  
1094 shown that  $T_e \approx T_i \approx T_n$  and that equations (15) and (16) are approximately  
1095 valid.

#### 1096 4. Discussion and Conclusions

1097 We have constructed a new model for the upper atmosphere of HD209458b  
1098 in order to explain the detections of H, O, C<sup>+</sup>, and Si<sup>2+</sup> at high altitudes  
1099 around the planet (Vidal-Madjar et al., 2003, 2004; Linsky et al., 2010).  
1100 There are many different interpretations of the observed transits in the H  
1101 Lyman  $\alpha$  line (Vidal-Madjar et al., 2003; Ben-Jaffel, 2007, 2008; Holström  
1102 et al., 2008; Koskinen et al., 2010a), and these interpretations rely on results  
1103 from models of the upper atmosphere that are based on many uncertain as-  
1104 sumptions (see Section 3.1.1 and Koskinen et al., 2010a, for a review). Also,  
1105 the detection of heavy atoms and ions in the thermosphere is not without

1106 controversy, and the detection of  $\text{Si}^{2+}$  is particularly intriguing. Thus these  
1107 observations present several interesting challenges to modelers.

1108 The observed transit depths are large, and substantial abundances of the  
1109 relevant species are required to explain the observations. However, on every  
1110 planet in the solar system heavier species are removed from the thermo-  
1111 sphere by molecular diffusion and doubly ionized species are not commonly  
1112 observed. Also, the observations imply that H and O remain mostly neutral  
1113 in the thermosphere while C and Si are mostly ionized at a relatively low  
1114 altitude. Hydrodynamic models coupled with chemistry and thermal struc-  
1115 ture calculations are required to explain the detection of these species in the  
1116 upper atmosphere and the differences between their density profiles. Ours is  
1117 the first such model that benefits from repeated detections of both neutral  
1118 atoms and ions to constrain the composition and temperature.

1119 Koskinen et al. (2010a) demonstrated that the H Lyman  $\alpha$  transit obser-  
1120 vations (Ben-Jaffel, 2007, 2008) can be explained with absorption by H in  
1121 the thermosphere if the base of the hot layer of H is near  $1 \mu\text{bar}$ , the mean  
1122 temperature within the layer is about 8,250 K, and the atmosphere is mostly  
1123 ionized above  $3 R_p$ . These parameters are based on fitting the data with  
1124 a simple empirical model of the upper atmosphere. The density and tem-  
1125 perature profiles from our new hydrodynamic model agree qualitatively with  
1126 these constraints, demonstrating that the basic assumptions of Koskinen et  
1127 al. (2010a) are reasonable. This confirms once again that a comet-like tail  
1128 (Vidal-Madjar et al., 2003) or energetic neutral atoms (Holström et al., 2008)



1129 are not necessarily required to explain the H Lyman  $\alpha$  observations.

1130 In line with recent results by Moses et al. (2011) and the empirical con-  
1131 straints mentioned above, we used a photochemical model of the lower atmo-  
1132 sphere to show that H<sub>2</sub> dissociates near the 1  $\mu$ bar level. Above this level,  
1133 the lack of efficient radiative cooling and strong stellar EUV heating lead  
1134 to high temperatures. We constrained the range of possible mean (pressure  
1135 averaged) temperatures based on the average solar flux by using the hydro-  
1136 dynamic model to calculate temperatures with different heating efficiencies.  
1137 For net heating efficiencies between 0.1 and 1, the mean temperature below  
1138  $3 R_p$  varies from 6,000 K to 8,000 K. This means that 8,000 K is a relatively  
1139 strict upper limit on the mean temperature if the XUV flux of HD209458 is  
1140 similar to the corresponding flux of the sun.

1141 A mean temperature of 8,250 K estimated from the observations implies  
1142 the presence of an additional non-radiative heat source, or that the XUV flux  
1143 from HD209458 is higher than the average solar flux. Given that our best  
1144 estimate of the net heating efficiency is 0.44 (see Section 3.1.2), the XUV flux  
1145 of HD209458 would have to be 5–10 times higher than the average solar flux to  
1146 cause a mean temperature of 8,250 K (see Section 3.1.1). If the mean XUV  
1147 flux of HD209458 is generally higher than the solar flux and the observations  
1148 took place during stellar maximum, such an enhancement is not impossible.  
1149 This would also lead to higher outflow velocity and mass loss rate. However,  
1150 the uncertainty in the observed transit depths is also large (Ben-Jaffel, 2008;  
1151 Ben-Jaffel and Hosseini, 2010), and it can accommodate a range of temper-

1152 atures. Therefore our reference model C2 with a mean temperature of 7,200  
1153 K also agrees qualitatively with the empirical constraints. In this respect, it  
1154 is interesting to note that with 100x solar flux, the mean temperature is still  
1155 only 9,800 K. Temperatures significantly higher than 8,000 K (e.g., Ben-Jaffel  
1156 and Hosseini, 2010) therefore imply a strong non-radiative heat source.

1157 In contrast to the mean temperature, the velocity and details of the tem-  
1158 perature profile depend strongly on the heating efficiency and stellar flux  
1159 (see Section 3.1.1). They are also sensitive to the upper and lower boundary  
1160 conditions. This explains the large range of temperature and density profiles  
1161 predicted by earlier models that arise from different boundary conditions and  
1162 assumptions about the stellar flux, radiative transfer, and heating efficiencies.  
1163 The differences highlight the need for accurate thermal structure calculations  
1164 that are constrained by the available observations. These calculations are im-  
1165 portant because the density profiles of the detected species depend on the  
1166 temperature and velocity profiles, and inappropriate assumptions made by  
1167 the models can bias the interpretation of the observations.

1168 In the absence of stellar gravity, the location of the sonic point and the  
1169 outflow speed also depend on the heating efficiency. As the heating efficiency  
1170 increases from 0.1 (in models with the average solar flux), the high altitude  
1171 temperature increases and the sonic point moves to lower altitudes, reaching  
1172 down to  $4 R_p$  with a net heating efficiency of 1. We found that supersonic  
1173 solutions are possible as long as there is significant heating over a large alti-  
1174 tude range above the temperature peak. This conclusion is supported both

1175 by the hydrodynamic model and new constraints from kinetic theory (Volkov  
1176 et al., 2011a,b). However, the isentropic sonic point of the C2 model is lo-  
1177 cated above the model domain. In principle, this is an interesting result but  
1178 it should be treated with caution. We used parameterized heating efficiencies  
1179 for low energy photons, and the location of the sonic point is very sensitive to  
1180 the temperature profile. Also, the stellar tide can enhance the escape rates at  
1181 the substellar and antistellar points. We did not include this effect because  
1182 it may produce horizontal flows that cannot be modeled in 1D.

1183 As long as the upper boundary is at a sufficiently high altitude, we found  
1184 that the results based on the outflow boundary conditions and modified Jeans  
1185 conditions are identical (see Section 3.1.5). This shows that our simulations  
1186 are roughly consistent with kinetic theory. An agreement between these two  
1187 types of boundary conditions on HD209458b is an interesting theoretical  
1188 result. It shows that the boundary conditions for hydrodynamic escape are  
1189 appropriate in this case. However, an upper boundary at  $16 R_p$  or higher  
1190 is not necessarily justified for other reasons because we did not consider the  
1191 effect of the possible planetary magnetic field, interaction of the atmosphere  
1192 with the stellar wind, or horizontal transport (e.g., Stone and Proga, 2009;  
1193 Trammell et al., 2011).

1194 We chose an upper boundary at a high altitude in order to preserve the  
1195 integrity of the solution in our region of interest below  $5 R_p$ . The purpose of  
1196 this work is to model energy deposition and photochemistry in this region.  
1197 These aspects are often simplified in more complex models to a degree that

1198 it may be difficult to separate the effect of multiple dimensions and other  
1199 complications from differences arising simply because of different assump-  
1200 tions about heating efficiencies and chemistry. Also, the uncertainty in the  
1201 observations does not necessarily justify the introduction of more free pa-  
1202 rameters to the problem until the basic properties of the thermosphere are  
1203 better understood. However, technically we do not consider our solutions  
1204 to be accurate far above 3–5  $R_p$ . Instead, our results provide robust lower  
1205 boundary conditions for more complex multidimensional models that char-  
1206 acterize the atmosphere outside the Roche lobe of the planet. Results from  
1207 such models can then be used to constrain the upper boundary conditions of  
1208 the 1D models further.

1209 In order to model the density profiles of the detected species in the iono-  
1210 sphere, we assumed solar abundances of the heavy elements (Lodders, 2003),  
1211 although this assumption can be adjusted as required to explain the obser-  
1212 vations (Paper II). As we already stated we found that  $\text{H}_2$ ,  $\text{H}_2\text{O}$ , and  $\text{CO}$   
1213 dissociate above the 1  $\mu\text{bar}$  level, releasing H, O, and C to the thermosphere  
1214 (see also Moses et al., 2011). We note that the detection of  $\text{Si}^{2+}$  in the upper  
1215 atmosphere implies that silicon does not condense into clouds of forsterite  
1216 and enstatite in the lower atmosphere as argued by e.g., Visscher et al. (2010).  
1217 The dominant Si species is then  $\text{SiO}$ , which dissociates at a similar pressure  
1218 level as the other molecules. In fact, practically all molecules dissociate below  
1219 0.1  $\mu\text{bar}$ . This leads to an important simplification in hydrodynamic models  
1220 of the thermosphere. The complex chemistry of molecular ions does not need

1221 to be included as long as the lower boundary is above the dissociation level.

1222 We found that the H/H<sup>+</sup> transition occurs near 3  $R_p$  or, depending on  
1223 the velocity profile, at even higher altitudes. The O/O<sup>+</sup> transition is coupled  
1224 to the H/H<sup>+</sup> transition through charge exchange reactions. Thus both H and  
1225 O are mostly neutral up to the boundary of the Roche lobe at 3–5  $R_p$ . In  
1226 contrast, C is ionized near the 1  $\mu$ bar level and C<sup>+</sup> is the dominant carbon  
1227 species in the thermosphere. Si is also ionized near the 1  $\mu$ bar level, and the  
1228 balance between Si<sup>+</sup> and Si<sup>2+</sup> is determined by charge exchange with H<sup>+</sup> and  
1229 H, respectively. Si<sup>+</sup> is the dominant silicon ion below 5  $R_p$  but the abundance  
1230 of Si<sup>2+</sup> is also significant. We found that neutral heavy atoms are dragged  
1231 to the thermosphere by the escaping H, while heavy ions are transported  
1232 efficiently by the escaping H<sup>+</sup>. Thus the advection timescale is much shorter  
1233 than the diffusion timescale of the detected species, and diffusive separation  
1234 does not take place in the thermosphere. We also verified that the neutral,  
1235 ion, and electron temperatures are roughly equal.

1236 Taken together, these results imply that the thermospheres of close-in  
1237 EGPs can differ fundamentally from the gas giant planets in the solar sys-  
1238 tem. For instance, the thermosphere of HD209458b is composed mainly of  
1239 atoms and atomic ions, and diffusive separation of the common heavy species  
1240 is prevented by the escape of H and H<sup>+</sup>. It is important to note, however,  
1241 that results such as these cannot be freely generalized to other extrasolar  
1242 planets. As in the solar system, each planet should be studied separately.  
1243 For instance, the dissociation of molecules depends on the temperature pro-

1244 file that is shaped by the composition through radiative cooling and stellar  
1245 heating. The mass loss rate and escape velocity, that determine whether dif-  
1246 fusive separation takes place or not, depends on the escape mechanism that  
1247 again depends on the temperature and composition of the upper atmosphere.  
1248 The results from different models can only be verified by observations that  
1249 are therefore required for multiple planets if we are to characterize escape in  
1250 different systems and under different conditions.

1251

1252 We are grateful to A. Volkov for reading the manuscript and providing  
1253 useful feedback. We thank H. Menager, M. Barthelemy, J.-M. Grießmeier,  
1254 N. Lewis, D. S. Snowden, and C. Cecchi-Pestellini for useful discussions and  
1255 correspondence. We also acknowledge the "Modeling atmospheric escape"  
1256 workshop at the University of Virginia and the International Space Science  
1257 Institute (ISSI) workshop organized by the team "Characterizing stellar and  
1258 exoplanetary environments" for interesting discussions and an opportunity  
1259 to present our work. The calculations for this paper relied on the High  
1260 Performance Astrophysics Simulator (HiPAS) at the University of Arizona,  
1261 and the University College London Legion High Performance Computing  
1262 Facility, which is part of the DiRAC Facility jointly funded by STFC and  
1263 the Large Facilities Capital Fund of BIS. SOLAR2000 Professional Grade  
1264 V2.28 irradiances are provided by Space Environment Technologies.

1265 **References**

- 1266 Aldrovandi, S. M. V., Pequignot, D., 1973. Radiative and dielectronic recom-  
1267 bination coefficients for complex ions. *Astron. Astrophys.*, 25, 137–140.
- 1268 Bastian, T. S., Dulk, G. A., Leblanc, Y., 2000. A search for radio emission  
1269 from extrasolar planets. *Astrophys. J.*, 545, 1058–1063.
- 1270 Batygin, K., Stevenson, D. J., 2010. Inflating hot Jupiters with Ohmic dissi-  
1271 pation. *Astrophys. J. Lett.*, 714, L238–L243.
- 1272 Ben-Jaffel, L. 2007. Exoplanet HD209458b: Inflated hydrogen atmosphere  
1273 but no sign of evaporation. *Astrophys. J. Lett.*, 671, L61–L64.
- 1274 Ben-Jaffel, L. 2008. Spectral, spatial, and time properties of the hydrogen  
1275 nebula around exoplanet HD209458b. *Astrophys. J.*, 688, 1352–1360.
- 1276 Ben-Jaffel, L., Hosseini, S. S., 2010. On the existence of energetic atoms in  
1277 the upper atmosphere of exoplanet HD209458b. *Astrophys. J.*, 709, 1284–  
1278 1296.
- 1279 Black, J. H., 1981. The physical state of primordial intergalactic clouds. *Mon.*  
1280 *Not. R. Astr. Soc.*, 197, 553–563.
- 1281 Carver, G. D., Brown, P. D., Wild, O., 1997. The ASAD atmospheric chem-  
1282 istry integration package and chemical reaction database. *Comp. Phys.*  
1283 *Comm.*, 105, 197–215.

- 1284 Cecchi-Pestellini, C., Ciaravella, A., Micela, G., Penz, T., 2009. The relative  
1285 role of EUV radiation and X-ray in the heating of hydrogen-rich exoplanet  
1286 atmospheres. *Astron. Astrophys.*, 496, 863–868.
- 1287 Chamberlain, J. W., 1961. Interplanetary gas. III. A hydrodynamic model of  
1288 the corona. *Astrophys. J.*, 133, 675–687.
- 1289 Chapman, S., Cowling, T. G., 1970. The mathematical theory of non-uniform  
1290 gases. Cambridge University Press, Cambridge, England.
- 1291 Charbonneau, D., Brown, T. M., Noyes, R. W., Gilliland, R. L. 2002. Detec-  
1292 tion of an extrasolar planet atmosphere. *Astrophys. J.*, 568, 377–384.
- 1293 Charbonneau, D., et al., 2009. A super-Earth transiting a nearby low-mass  
1294 star. *Nature*, 462, 891–894.
- 1295 Coustenis, A. et al., 1998. High resolution ground-based spectroscopy of 51  
1296 Peg b: Search for atmospheric signatures. *Brown dwarfs and extrasolar*  
1297 *planets*, ASP Conf. Ser., 134, 296–303.
- 1298 Erkaev, N. V., et al., 2007. Roche lobe effects on the atmospheric loss from  
1299 ”Hot Jupiters”. *Astron. Astrophys.*, 472, 329–334.
- 1300 Garcia Munoz, A. 2007. Physical and chemical aeronomy of HD209458b.  
1301 *Plan. Sp. Sci.*, 55, 1426–1455.
- 1302 Glover, S. C. O., Jappsen, A.-K., 2007. Star formation at very low metallicity.  
1303 I. Chemistry and cooling at low densities. *Astrophys. J.*, 666, 1–19.



- 1304 Gombosi, T. I., 1994. *Gaskinetic theory*. Cambridge University Press, Cam-  
1305 bridge, England.
- 1306 Guo, J. H., 2011. Escaping particle fluxes in the atmospheres of close-in  
1307 exoplanets. I. Model of hydrogen. *Astrophys. J.*, 733, 98.
- 1308 Grißmeier, J.-M., et al., 2007. Predicting low-frequency radio fluxes of  
1309 known extrasolar planet. *Astron. Astrophys.*, 475, 359–368.
- 1310 Grißmeier, J.-M., Zarka, P., Girard, J. N., 2011. Observation of planetary  
1311 radio emissions using large arrays. *Rad. Sci.*, 46, RS0F09.
- 1312 Holström, M., Ekenback, A, Selsis, F., Lammer, H., Wurz, P., 2008. Energetic  
1313 neutral atoms as the explanation for the high-velocity hydrogen around  
1314 HD209458b. *Nature*, 451, 970–972.
- 1315 Hummer, D. G., Seaton, M. J., 1963. The ionization structure of planetary  
1316 nebulae. *Mon. Not. R. Astron. Soc.*, 125, 437–459.
- 1317 Hunten, D. M., 1973. The escape of light gases from planetary atmospheres.  
1318 *J. Atmos. Sci.*, 30, 1481–1494.
- 1319 Hunten, D. M., Pepin, R. O., Walker, J. C. G., 1987. Mass fractionation in  
1320 hydrodynamic escape. *Icarus*, 69, 532–549.
- 1321 Jacobson, M. Z., 1999. *Fundamentals of atmospheric modeling*. Cambridge  
1322 University Press, Cambridge, England.

- 1323 Jaritz, G. F., et al., 2005. Roche lobe effects on expanded upper atmospheres  
1324 of short-periodic giant exoplanets. *Astron. Astrophys.*, 439, 771–775.
- 1325 Kingdon, J. B., Ferland, G. J., 1996. Rate coefficients for charge transfer  
1326 between hydrogen and the first 30 elements. *Astrophys. J. Supp.*, 106,  
1327 205–211.
- 1328 Knutson, H. A., Charbonneau, D., Allen, L. E., Burrows, A., Megeath, S.  
1329 T., 2008. The 3.6–8.0  $\mu\text{m}$  broadband emission spectrum of HD209458b:  
1330 Evidence for an atmospheric temperature inversion. *Astrophys. J.*, 673,  
1331 526–531.
- 1332 Koskinen, T. T., Aylward, A. D., Miller, S., Smith, C. G. A., 2007a. A  
1333 thermospheric circulation model for extrasolar giant planets. *Astrophys.*  
1334 *J.*, 661, 515–526.
- 1335 Koskinen, T. T., Aylward, A. D., Miller, S., 2007b. A stability limit for the  
1336 atmospheres of giant extrasolar planets. *Nature*, 450, 845–848.
- 1337 Koskinen, T. T., Aylward, A. D., Miller, S., 2009. The upper atmosphere of  
1338 HD17156b. *Astrophys. J.*, 693, 868–885.
- 1339 Koskinen, T. T., Yelle, R. V., Lavvas, P., Lewis, N., 2010a. Characterizing  
1340 the thermosphere of HD209458b with UV transit observations. *Astrophys.*  
1341 *J.*, 723, 116–128.
- 1342 Koskinen, T. T., Cho, J. Y-K., Achilleos, N., Aylward, A. D., 2010b. Ioniza-  
1343 tion of extrasolar giant planet atmospheres. *Astrophys. J.*, 722, 178–187.

- 1344 Koskinen, T. T., Harris, M., Yelle, R. V., Lavvas, P., 2012. The escape of  
1345 heavy atoms from the ionosphere of HD209458b. II. Interpretation of the  
1346 observations. *Icarus*, *submitted*
- 1347 Lammer, H., et al., 2003. Atmospheric loss of exoplanets resulting from stellar  
1348 X-ray and extreme-ultraviolet heating. *Astrophys. J. Lett.*, 598, L121–  
1349 L124.
- 1350 Lammer, H., et al., 2009. Determining the mass loss limit for close-in exo-  
1351 planets: What can we learn from transit observations? *Astron. Astrophys.*,  
1352 506, 399–410.
- 1353 Lavvas, P., Coustenis, A., Vardavas, I. M., 2008a. Coupling photochemistry  
1354 with haze formation in Titan’s atmosphere, part I: Model description. *Plan.*  
1355 *Space Sci.*, 56, 27–66.
- 1356 Lavvas, P., Coustenis, A., Vardavas, I. M., 2008b. Coupling photochemistry  
1357 with haze formation in Titan’s atmosphere, part II: Results and validation  
1358 with Cassini/Huygens data. *Plan. Space Sci.*, 56, 67–99.
- 1359 Lazio, T. J. W., Farrell, W. M., 2007. Magnetospheric emissions from the  
1360 planet orbiting  $\tau$  Bootis: A multiepoch search. *Astrophys. J.*, 668, 1182–  
1361 1188.
- 1362 Lecavelier des Etangs, A., Vidal-Madjar, A., McConnell, J. C., Hébrard,  
1363 G., 2004. Atmospheric escape from hot Jupiters. *Astron. Astrophys.*, 418,  
1364 L1–L4.

- 1365 Lecavelier des Etangs, A., 2007. A diagram to determine the evaporation  
1366 status of extrasolar planets. *Astron. Astrophys.*, 461, 1185–1193.
- 1367 Lecavelier des Etangs, A., Sirothia, S. K., Gopal-Khrisna, Zarka, P., 2011.  
1368 GMRT search for 150 MHz radio emissions from the transiting extrasolar  
1369 planets HD189733b and HD209458b. *Astron. Astrophys.*, 533, A50.
- 1370 Lemaire, J., Scherer, M., 1971a. Simple model for an ion exosphere in an  
1371 open magnetic field. *Phys. Fluids*, 14, 1683–1694.
- 1372 Lemaire, J., Scherer, M., 1971b. Kinetic models of the solar wind. *J. Geophys.*  
1373 *Res.*, 76, 7479–7490.
- 1374 Lemaire, J., Scherer, M., 1973. Kinetic models of the solar and polar winds.  
1375 *Rev. Geophys. Space Phys.*, 11, 427–468.
- 1376 Lemaire, P., et al., 2005. Variation of the full Sun hydrogen Lyman profiles  
1377 through solar cycle 23. *Adv. Space Sci.*, 35, 384–387.
- 1378 Linsky, J. L., et al. 2010. Observations of mass loss from the transiting exo-  
1379 planet HD209458b. *Astrophys. J.*, 717, 1291–1299.
- 1380 Lodders, K., Fegley, B. Jr., 2002. Atmospheric chemistry in giant planets,  
1381 brown dwarfs, and low-mass dwarf stars. I. Carbon, nitrogen, and oxygen.  
1382 *Icarus*, 155, 393–424.
- 1383 Lodders, K., 2003. Solar system abundances and condensation temperatures  
1384 of the elements. *Astrophys. J.*, 591, 1220–1247.

- 1385 Mayor, M., Queloz, D., 1995. A Jupiter-mass companion to a solar-type star.  
1386 Nature, 378, 355–359.
- 1387 Menager, H., Barthelemy, M., Koskinen, T., Lilensten, J., 2011. Calculation  
1388 of the contrast between the emission of a hot Jupiter and its parent star  
1389 in H Lyman  $\alpha$ . *EPSC-DPS Joint Meeting*, 1, 581.
- 1390 Moses, J. I., et al., 2011. Disequilibrium carbon, oxygen, and nitrogen chem-  
1391 istry in the atmospheres of HD189733b and HD209458b. *Astrophys. J.*,  
1392 737, 15.
- 1393 Murray-Clay, R. A., Chiang, E. I., Murray, N., 2009. Atmospheric escape  
1394 from Hot Jupiters. *Astrophys. J.*, 693, 23–42.
- 1395 O’Neill, M. E., Chorlton, F., 1989. *Viscous and compressible fluid dynamics*.  
1396 Ellis Horwood Limited, Chichester, England.
- 1397 Opik, E. J., 1963. Selective escape of gases. *Geophys. J. Roy. Astron. Soc.*,  
1398 7, 490–509.
- 1399 Parker, E. N., 1958. Dynamics of the interplanetary gas and magnetic fields.  
1400 *Astrophys. J.*, 128, 664–676.
- 1401 Parker, E. N., 1965. Dynamical properties of stellar coronas and stellar winds.  
1402 IV. The separate existence of subsonic and supersonic solutions. *Astrophys.*  
1403 *J.*, 141, 1463–1478.

- 1404 Penz, T., et al., 2008. Mass loss from "Hot Jupiters" – Implications for  
1405 CoRoT discoveries, part II: Long time thermal atmospheric evaporation  
1406 modeling. *Plan. Space Sci.*, 56, 1260–1272.
- 1407 Ribas, I., Guinan, E. F., Güdel, M., Audard, M., 2005. Evolution of the solar  
1408 activity over time and effects on planetary atmospheres. I. High-energy  
1409 irradiances (1–1700 Å). *Astrophys. J.*, 622, 680–694.
- 1410 Sanz-Forcada, J., et al., 2010. A scenario of planet erosion by coronal radia-  
1411 tion. *Astron. Astrophys. Lett.*, 511, L8.
- 1412 Schneider, E. M., Velázquez, P. F., Esquivel, A., Rage, A. C., 2007. Three-  
1413 dimensional hydrodynamical simulation of the exoplanet HD209458b. *As-  
1414 trophys. J. Lett.*, 671, L57–L60.
- 1415 Schunk, R. W., Nagy, A. F., 2000. *Ionospheres: Physics, plasma physics, and  
1416 chemistry*. Cambridge University Press, Cambridge, England.
- 1417 Schneider, J., Rauer, H., Lasota, J. P., Bonazzola, S., Chassefiere, E., 1998.  
1418 The cometary tail of giant extrasolar planets at small orbital distances.  
1419 *Brown dwarfs and extrasolar planets*, ASP Conf. Ser., 134, 241–244.
- 1420 Shapiro, R., 1970. Smoothing, filtering, and boundary effects. *Rev. Geophys.*  
1421 *Space Phys.*, 8, 359–387.
- 1422 Sing, D. K., Vidal-Madjar, A., Desert, J.-M., Lecavelier des Etangs, A.,  
1423 Ballester, G., 2008a. Hubble Space Telescope STIS optical transit trans-  
1424 mission spectra of the hot Jupiter HD209458b. *Astrophys. J.*, 686, 658–666.

- 1425 Sing, D. K., et al., 2008b. Determining atmospheric conditions at the termi-  
1426 nator of the hot Jupiter HD209458b. *Astrophys. J.*, 686, 667–673.
- 1427 Showman, A., et al., 2009. Atmospheric circulation of hot Jupiters: Coupled  
1428 radiative-dynamical general circulation model simulations of HD189733b  
1429 and HD209458b. *Astrophys. J.*, 699, 564–584.
- 1430 Silva-Valio, A., 2008. Estimating stellar rotation from starspot detection dur-  
1431 ing planetary transits. *Astrophys. J.*, 683, L179–L182.
- 1432 Stancil, P. C., Havener, C. C., Krstic, P. S., Schultz, D. R., 1998. Charge  
1433 transfer in collisions of  $C^+$  with H and  $H^+$  with C. *Astrophys. J.*, 502,  
1434 1006–1009.
- 1435 Stone, J. M., Proga, D., 2009. Anisotropic winds from close-in extrasolar  
1436 planets. *Astrophys. J.*, 694, 205–213.
- 1437 Storey, P. J., Hummer, D. G., 1995. Recombination line intensities for hy-  
1438 drogenic ions - IV. Total recombination coefficients and machine-readable  
1439 tables for  $Z = 1$  to 8. *Mon. Not. R. Astron. Soc.*, 272, 41–48.
- 1440 Swain, M. R., et al., 2009. Water, methane, and carbon dioxide present in  
1441 the dayside spectrum of the exoplanet HD209458b. *Astrophys. J.*, 704,  
1442 1616–1621.
- 1443 Swartz, W. E., Nisbet, J. S., Green, A. E. S., 1971. Analytic expression  
1444 for the energy-transfer rate from photoelectrons to thermal-electrons. *J.*  
1445 *Geophys. Res.*, 76, 8425–8426.

- 1446 Tarter, J. C., et al., 2007. A reappraisal of the habitability of planets around  
1447 M dwarf stars. *Astrobiology*, 7, 30–65.
- 1448 Tian, F., Toon, O. B., Pavlov, A. A., de Sterck, H., 2005. Transonic hy-  
1449 drodynamic escape of hydrogen from extrasolar planetary atmospheres.  
1450 *Astrophys. J.*, 621, 1049–1060.
- 1451 Trammell, G. B., Arras, P., Li, Z.-Y., 2011. Hot Jupiter magnetospheres.  
1452 *Astrophys. J.*, 728, 152.
- 1453 Tobiska, W. K., et al., 2000. The SOLAR2000 empirical solar irradiance  
1454 model and forecast tool. *J. Atmos. Sol.-Terr. Phys.*, 62, 1233–1250.
- 1455 van Leer, B., 1979. Towards the ultimate flux conservative difference scheme.  
1456 V. A second-order sequel to Godunov’s method. *J. Comp. Phys.*, 32, 101–  
1457 136.
- 1458 Verner, D. A., Ferland, G. J., Korista, K. T., Yakolev, D. G., 1996. Atomic  
1459 data for astrophysics. II. New analytic fits for photoionization cross sections  
1460 of atoms and ions. *Astrophys. J.*, 465, 487–498.
- 1461 Vidal-Madjar, A., et al., 2003. An extended upper atmosphere around the  
1462 extrasolar giant planet HD209458b. *Nature*, 422, 143–146.
- 1463 Vidal-Madjar, A., et al., 2004. Detection of oxygen and carbon in the hy-  
1464 drodynamically escaping atmosphere of the extrasolar planet HD209458b.  
1465 *Astrophys. J. Lett.*, 604, L69–L72.



- 1466 Vidal-Madjar, A., et al., 2011a. The upper atmosphere of the exoplanet  
1467 HD209458b revealed by the sodium D lines: Temperature–pressure pro-  
1468 file, ionization layer, thermosphere. *Astron. Astrophys.*, 527, A110.
- 1469 Vidal-Madjar, A., et al., 2011b. The upper atmosphere of the exoplanet  
1470 HD209458b revealed by the sodium D lines: Temperature–pressure profile,  
1471 ionization layer, thermosphere (Corrigendum). *Astron. Astrophys.*, 533,  
1472 C4.
- 1473 Visscher, C., Lodders, K., Fegley, B., Jr., 2010. Atmospheric chemistry in gi-  
1474 ant planets, brown dwarfs, and low-mass dwarf stars. III. Iron, magnesium,  
1475 and silicon. *Astrophys. J.*, 716, 1060–1075.
- 1476 Volkov, A. N., Johnson, R. E., Tucker, O. J., Erwin, J. T., 2011a. Thermally  
1477 driven atmospheric escape: Transition from hydrodynamic escape to Jeans  
1478 escape. *Astrophys. J. Lett.*, 729, L24.
- 1479 Volkov, A. N., Tucker, O. J., Erwin, J. T., Johnson, R. E., 2011b. Kinetic  
1480 simulations of thermal escape from a single component atmosphere. *Phys.*  
1481 *Fluids*, 23, 066601.
- 1482 Voronov, G. S., 1997. A practical fit formula for ionization rate coefficients  
1483 of atoms and ions by electron impact:  $Z = 1$ –28. *Atom. Data Nucl. Data*,  
1484 65, 1–35
- 1485 Waite, J. H. Jr., et al., 1983. Electron precipitation and related aeronomy of

- 1486 the Jovian thermosphere and ionosphere. *J. Geophys. Res.*, 88, A86143–  
1487 A86163.
- 1488 Watson, A. J., Donahue, T. M., Walker, J. C. G., 1981. The dynamics of a  
1489 rapidly escaping atmosphere: Applications to the evolution of Earth and  
1490 Venus. *Icarus*, 48, 150–166.
- 1491 Woodall, J., Agundez, M., Marwick-Kemper, A. J., Millar, T. J., 2007. The  
1492 UMIST database for astrochemistry 2006. *Astron. Astrophys.*, 466, 1197–  
1493 1204.
- 1494 Woods, T. N., Rottman, G. J., 2002. Solar ultraviolet variability over time pe-  
1495 riods of aeronomical interest. In: Mendillo, M., et al. (Eds.), *Comparative*  
1496 *aeronomy in the solar system*. American Geophysical Union Monograph.
- 1497 Yan, M., Sadeghpour, H. R., Dalgarno, A., 1998. Photoionization cross sec-  
1498 tion of He and H<sub>2</sub>. *Astrophys. J.*, 496, 1044–1050.
- 1499 Yelle, R. V., 2004. Aeronomy of extra-solar giant planets at small orbital  
1500 distances. *Icarus*, 170, 167–179.
- 1501 Yelle, R. V., Miller, S., 2004. Jupiter’s thermosphere and ionosphere. *Jupiter*  
1502 *– the planet, satellites and magnetosphere*. Cambridge University Press,  
1503 Cambridge, England.
- 1504 Yelle, R. V., 2006. Corrigendum to ”Aeronomy of extra-solar giant planets  
1505 at small orbital distances”. *Icarus*, 183, 508.

1506 Zahnle, K. J., Kasting, J. F., 1986. Mass fractionation during transonic es-  
1507 cape and its implications for loss of water from Mars and Venus. *Icarus*,  
1508 68, 462–480.

1509 Zhanle, K., Marley, M. S., Freedman, R. S., Lodders, K., Fortney, J. J., 2009.  
1510 Atmospheric sulfur photochemistry on hot Jupiters. *Astrophys. J. Lett.*,  
1511 701, L20–L24.